1

Received by OSTI

NOV 0 7 1986

TITLE: THREE DIMENSIONAL NUMERICAL SIMULATIONS OF THE UPS-292-SC ENGINE

AUTHOR(S): Peter J. O'Rourke and Anthony A. Amsden

DISCLAIMER

Los Alamos

Los Alamos National Laboratory
Los Alamos, New Mexico 87545

MASTER

1C/14/86

THREE DIMENSIONAL NUMERICAL SIMULATIONS OF THE UPS-292-SC ENGINE

By

Peter J. O'Rourke and Anthony A. Amsden

ABSTRACT

We present and analyze three-dimensional calculations of the spray, mixing and combustion in the UPS-292 stratified charge engine for three different operating conditions, corresponding to overall air-fuel ratios between 22.4 and 61.0. The numerical calculations are performed with KIVA, a multidimensional arbitrary-mesh, finite-difference hydrodynamics program for internal combustion engine applications. The calculations use a mesh of 10,000 computational cells, which conform to the shape of the piston bowl and cylinder and move to follow piston motion. Each operating condition is calculated from intake valve closure at 118° BTDC to 90° ATDC and requires approximately three hours of CRAY-XMP computer time.

Combustion occurs primarily in wake of the spark plug, and to include the effects of the spark plug on the flow field, we use a novel internal obstacle treatment. The methodology, in which internal obstacles are represented by computational particles, promises to be applicable to the calculation of the flows around intake and exhaust valves.

Comparisons are made of several computed and measured quantities. Pressure histories compare well at the highest load conditions. Computed emissions of NO agree well with experiment, but those of HC and CO agree poorly. Predicted wall heat losses are approximately two-thirds of the measured values for all test conditions. Computed combustion efficiencies compare poorly with experiment. We discuss the reasons for agreement or disagreement and tell how the results change when some of the controlling physical parameters are varied.

The calculations also yield much information that is not obtainable experimentally. Plots are given of the histories of the following global quantities: liquid fuel mass, fuel vapor mass, fuel vapor mass in premixed regions, chemical heat release, wall heat loss, pressure work done on the piston, and the masses of several gas species. In addition, we analyze plots of velocities, temperature, and concentrations at various times, and describe a computer-generated movie that helps visualize the complex three-dimensional flow fields.

I. INTRODUCTION

In the past several years rapid progress has been made in multidimensional modeling of the flow and combustion in internal combustion engines, both in terms of the speed and accuracy of numerical methods and in terms of the accuracy of submodels for the controlling physical processes. Excellent reviews are available that cover various aspects of the origin and development of multidimensional models (1-6). Approximately ten years ago the first calculations were performed of two-dimensional laminar flame propagation (7,8). Today, many calculations have been reported of two-dimensional engine flows with sprays and combustion and of three-dimensional cold flows in engines (9-12). Until now, however, a major goal of the engine modeling effort has not been realized: the calculation of three-dimensional engine flows with combustion and sprays. It is the purpose of this paper to report that such calculations can now be economically performed and to compare computed three-dimensional results with experimental measurements of a stratified charge internal combustion engine.

The main reason three-dimensional engine combustion simulations have not been performed is that the computer times for these calculations have been prohibitively long. Based on the increased number of computational cells required, the extension from two dimensions to three dimensions requires at least an order of magnitude increase in computer time. Including combustion increases computer time by at least another factor of two, based on the number of equations solved. This is because in order to compute pressures accurately during hydrocarbon combustion, one must keep track of approximately ten chemical species and integrate an equal number of chemical rate equations. In addition, many of the chemical reactions are fast and require time-consuming stiff equation solvers. Calculating liquid sprays can also significantly increase computational time. The accurate calculation of spray dynamics requires the solution of the spray equation. This is a stochastic equation for the evolution of the probability distribution f of droplet locations, velocities,

sizes, and temperatures (13). In three dimen-
sions, f has at least eight independent
variables.

The calculations of this paper were per-
formed with the KIVA computer program (14,15).
The main capabilities of KIVA are described in
the next section of this paper, but here we
briefly mention three features of KIVA that
greatly increase its computational efficiency
for multidimensional engine combustion calcu-
lations. First, insofar as is possible the
computer program takes advantage of the vector
calculation capability of the CRAY computer.
Second, fast methods are used for calculating
chemical equilibria in post-flame gases
(16,17). Third, a very efficient stochastic
particle method is used to solve the spray
equation (18).

The calculations are compared with exper-
imental measurements in the UPS-292 stratified
charge engine (19-21). In response to the en-
ergy crisis of the 1970's, the United Parcel
Service launched a research program into a
multifuel stratified charge engine. They have
developed an engine that increases the fuel
efficiency of the GM 292 six-cylinder engine
by 25 to 35 percent, has low pollutant emis-
sions, and can burn a variety of fuels. A
major purpose of this paper is to investigate
how the UPS engine accomplishes these
objectives.

After describing the KIVA computer pro-
gram, we give the conditions and results of
experiments performed at General Motors
Research Laboratories (22). Next we give the
computational parameters that were used to
simulate the experiments, and then the compu-
tational results are described and compared
with the experiments. We also discuss some
calculations to test the sensitivity of the
results to computational parameter variations.
Finally, we analyze plots of the detailed flow
field and describe a computer-generated movie
that helps one understand the three-dimension-
al dynamics of the spray, mixing, and
combustion.

II. THE NUMERICAL MODEL

In this section we describe the general
features of the numerical model and cite its

strengths and weaknesses. Details of the
model can be found in several recent publica-
tions (14,15,23,24). The KIVA computer pro-
gram solves the three-dimensional, unsteady
equations of motion of a chemically reactive
mixture of ideal gases. It can also solve for
the dynamics of a liquid fuel spray and the
coupling between the spray and the gas.

The gas phase equations are solved by
using finite difference approximations on a
computational mesh composed of arbitrary hexa-
hedrons. The arbitrary mesh can conform to
curved boundaries and can move to follow
changes in combustion chamber geometry. A
strength of the method is that there are no
geometrical restrictions on the mesh; in par-
ticular, the mesh need not be orthogonal.
Another strength of the method is that the
same computer program can be used to calculate
efficiently flows of arbitrary Mach number.
In low Mach number problems, an acoustic sub-
cycling method is used to improve computation-
al efficiency (25).

Chemically, KIVA can solve continuity
equations for an arbitrary number of species
undergoing an arbitrary number of chemical re-
actions, restricted only by computer storage
and time requirements. Chemical reactions are
divided into finite-rate and equilibrium reac-
tions. Two implicit equation solvers are
available to compute chemical equilibria -- a
fast algebraic solver for hydrocarbon/air com-
bustion (16) and an iterative solver for more
general circumstances (17).

A standard k-ε turbulence model has been
installed in the computer program (26), and
this was used for the calculations of this
paper. Although widely used in combustion
simulations, this turbulence model is defi-
cient in at least two respects, in that it
neglects the effects of counter-gradient
transport (27) and of flow streamline cur-
vature (28).

We have also neglected the effects of
turbulence/chemistry interactions (29). Chem-
ical conversion rates are given by laminar
Arrhenius expressions with turbulent mean flow
quantities used in place of laminar values.
Although such reaction rates can be adjusted
to give experimentally observed average con-
version rates, the detailed variations in

chemical reaction rates in space and time will
not be accurately predicted using our model.
In this respect the current model is not pre-
dictive because the reaction rate must be ad-
justed to give the average burning rate ob-
served in the experiment. Simple models are
available for turbulence/chemistry interac-
tions (9,26), and these would not significant-
ly increase the computer times of the calcula-
tions of this paper.

As with the k-ε turbulence model, the
wall heat loss submodel in KIVA is widely used
but may need modifications for engine calcula-
tions. In our model, the velocities at grid
points closest to walls are matched to a tur-
bulent law-of-the-wall velocity profile, and
the wall shear stress is deduced from this.'
The wall heat loss is then obtained by a
Reynolds analogy formula. The model is appro-
priate for steady, incompressible boundary
layers on flat surfaces but may need modifica-
tions to account for the effects of unsteadi-
ness, compressibility, and streamline curva-
ture. In addition, a practical question
arises concerning our ability to resolve wall
regions well enough to have a grid point in
the law-of-the-wall region.

The spray model is probably the best
tested submodel of KIVA, both in terms of nu-
merical accuracy and comparisons with experi-
ments (30). The liquid fuel spray is calcu-
lated by a stochastic particle technique (18).
The model calculates the complete coupling be-
tween the liquid and gas due to mass, momen-
tum, and energy exchanges. Also included are
the effects of droplet collisions and coales-
cences, which are important in many practical
sprays (31). One weakness in the model is the
need to specify the drop sizes and spray
angles that result from liquid jet atomiza-
tion. A complete understanding of liquid jet
atomization is lacking, although guidance is
available from experiments that indicate atom-
ization is primarily caused by aerodynamic in-
teraction of the gas and liquid (32). Recent
promising research (33) supports the conclu-
sion that by incorporating a model for droplet
aerodynamic break-up, correct droplet sizes
can be predicted without knowing the details
of the atomization process. If this is true,

a major weakness of the spray model can be
elimirated.

III. THE EXPERIMENTAL CONDITIONS AND RESULTS

The experiments described in this section
were performed at General Motors Research
Laboratories (22). The geometry of the UPS-
292-SC engine is drawn to scale in Fig. 1, and
some of its dimensions are given in Table 1.

TABLE 1
UPS-292-SC ENGINE GEOMETRY

Bore	9.843 cm
Stroke	10.46 cm
Connecting Rod	17.186 cm
Compression Ratio	13:1
Bowl Volume	54.8 cm^3
Bowl Diameter	5.05 cm
Squish Height	0.13 cm
Ring Land Volume	1.6 cm^3
Head	Flat

Figure 1 shows the piston at top-dead-center.
At this time the squish height is so small
that the piston bowl effectively is the com-
bustion chamber. Also depicted are two scal-
lops in the piston bowl. The larger of these
accommodates the spark plug near top-dead-
center, and the smaller accommodates the
liquid fuel injector.

The events occurring in the experimental
UPS engine during injection and combustion are
depicted schematically in Fig. 2. The swirl
number at intake valve closure is 6.5. Igni-
tion and injection begin simultaneously.
Ignition is by a spark plug that sparks con-
tinuously for 35° crank angle. The fuel spray
is injected cocurrently with the swirl and is
directed at the tip of the spark plug. Some
characteristics of the injector are given in
Table 2.

TABLE 2

INJECTOR CHARACTERISTICS

Tip	Conical seat emptying into a small sack with a 0.048 cm diameter hole
Inlet hole L/D	1.105
Δp	2000 psi nominal

The fuel used in the experiments is Amoco 91 gasoline at a temperature of 358 K. The H/C ratio of this fuel is 1.85, and its lower heating value is 43.67 MJ/kg.

Three different operating conditions were tested, and these are given in Table 3. The engine speed was 2000 rpm for all the tests.

TABLE 3

ENGINE TEST CONDITIONS

Case	1	2	3
Mass Injected (mg)	31.3	20.8	12.3
Injection & Ignition Timing (°BTDC)	26	19.3	17.5
Injection Duration (°)	25	20	15
Trapped Mass (mg)	807.4	847.6	849.5
Overall Air-Fuel Ratio	22.4	35.2	61.0
Head Temperature (K)	406	394	379
Liner Temperature	390	380	369
Piston Temperature	430	418	400
Exhaust Valve Temperature	1200	875	600

The main quantities varied were the mass of injected fuel and the injection timing and duration. The injection event was delayed and shortened when less fuel was injected.

The experimentally measured quantities were the in-cylinder pressure history and the composition and temperature of the exhaust gases. From these quantities, the wall heat

loss was inferred from a thermodynamic analysis of the engine (22). The experimental pressure histories will be given in the computational results section of this paper. The remaining experimentally measured quantities are given in Table 4. An interesting trend is that with decreasing load, hydrocarbon emissions increase and, correspondingly, combustion efficiency decreases.

TABLE 4

EXPERIMENTAL RESULTS

Case	1	2	3
NO_x (ppm)	1029	332	117
HC (C_6ppm)	17.8	236	452
CO (%)	0.282	0.108	0.078
O_2	6.85	12.8	16.2
CO_2	9.79	5.42	2.92
H_2O	8.5	5.0	2.9
N_2	74.5	76.6	77.8
Bosch Smoke Number	4.1	0.4	0.0
Combustion Efficiency	98.2	96.1	89.2
Heat Loss (J)	213.2	161.2	132.6
Exhaust Temperature (K)	933.	703.	538.

Figure 2 also depicts the events thought to occur during the combustion phase of the UPS engine cycle. The incompletely vaporized spray is ignited by the spark plug, and a stationary flame front forms in the wake of the plug. The flame remains attached to the spark plug because of the continuous spark and because of the slowing of the swirling flow near the plug. Combustion products are swept downstream by the swirling flow, but based on the swirl ratio and the duration of injection and ignition, injection is complete before the burn products have been swept once around the combustion chamber. The results of the numerical model will greatly modify and supplement this scenario for the combustion event.

IV. COMPUTATIONAL PARAMETERS

In this section we give the computational parameters used to simulate the three operating conditions of the UPS-292 engine. All calculations commence at intake value closure at 118° BTDC and terminate at a crank angle of 92° ATDC. Figure 3 shows three views of the computational mesh at 53° BTDC, including the positions of computational particles that are used to represent the spark plug. Later we will describe in detail how we include the effects of the spark plug on the flow field. The mesh has 22 cells in the radial direction, 18 in the azimuthal direction, and 22 cells in the axial direction. In order to form the piston bowl, all cells in an annulus composed of the outer ten cells radially and lower twelve cells axially are taken to be obstacle cells lying inside the piston. Some cells in the piston bowl and below the spark plug are deformed to conform to the shape of the scallop into which the spark plug fits near top-dead-center, as is shown in Fig. 4.

Figure 4 also shows that near top-dead-center only two planes of cells remain above the piston face. As the piston moves upward, the axial dimension of cells above the piston face decreases. Each time this axial dimension becomes less than a small predetermined value, we delete one plane of cells above the piston and map the flow field onto the new mesh. This procedure improves computational efficiency by maximizing the cell axial dimension, and at the same time reducing the number of cells. Conversely, the deleted planes are restored after top-dead-center when the piston is going back down. Cells lying in the piston bowl are simply translated with the piston motion.

At the boundaries of the computational domain, heat and momentum losses are calculated by assuming boundary layers are turbulent and matching to a law-of-the-wall velocity profile. The details of this procedure are given in the KIVA report (14). The wall temperatures, which are held constant in time but vary with wall position, are given in Table 1 of the engine parameters section.

The initial swirl velocities are related to the distance r from the cylinder axis by

$$w(r) = U_t J_1\left(\lambda \frac{r}{R}\right) \quad , \qquad (1)$$

where J_1 is the first order Bessel function, R is the cylinder radius, and λ is a constant with a value of 3.11. The form of this profile and the value of λ are taken from experimental measurements of swirling flows in cylinders (34). The value of U_t is taken to be

$$U_t = \frac{SR * \Omega * R * \lambda}{4 * J_2(\lambda)} \qquad (2)$$

where SR is the swirl ratio (6.5), Ω is the engine angular velocity in radians per second (RPM*2π/60), and J_2 is the Bessel function of order 2. This value of U_t gives the same angular momentum as a solid body swirl with angular velocity SR*Ω.

The initial masses of each species are inferred from reported values of trapped mass, injected fuel mass, air/fuel ratio, and exhaust gas composition. These initial masses are given in Table 5.

TABLE 5

INITIAL SPECIES MASSES (mg)
AND CYLINDER TEMPERATURE (K)

Case	1	2	3
M_{N_2}	592.198	632.633	641.667
M_{O_2}	159.380	173.189	179.144
M_{CO_2}	14.354	12.451	10.040
M_{H_2O}	9.881	8.393	6.272
M_{CO}	0.212	0.102	0.068
M_{NO}	0.077	0.031	0.010
Initial Temperature	384.6	361.9	356.7

The initial densities are assumed to be uniform and are found by dividing the masses in Table 5 by the volume of the computational region at intake valve closure. The initial temperature was computed from the ideal gas equation of state using these densities and the experimentally reported pressure.

To calculate the dynamics of the spray, the model requires the radii and velocities of the droplets at the injector. The magnitude of the injection velocity V_{inj} is determined from

$$V_{inj} = \frac{m_{inj}}{\rho_f \pi r_{inj}^2 t_{inj}} , \qquad (3)$$

where m_{inj} is the injected fuel mass, ρ_f the fuel density, r_{inj} the injector nozzle radius, and t_{inj} the injection duration. The Sauter mean radius r_{32} of the injected drops is then found from the formula

$$r_{32} = k \frac{\alpha}{\rho_g V_{inj}^2} , \qquad (4)$$

where α is the surface tension coefficient of the fuel, ρ_g the gas density at injection, and k is a constant taken to be 17.3. This formula and the value of k are predicted by an aerodynamic theory of liquid jet break-up (31). The injected drop radii are distributed according to

$$P(r) \ dr = \frac{1}{\bar{r}} e^{-r/\bar{r}} \ dr , \qquad (5)$$

where $\bar{r} = r_{32}/3$ and $P(r) \ dr$ is the probability that an injected drop has a radius between r and $r + dr$. The spray droplets are injected in a cone whose half-angle $\theta/2$ is determined from

$$\tan \frac{\theta}{2} = .95 \sqrt{\frac{\rho_g}{\rho_f}} . \qquad (6)$$

This formula has been experimentally verified for sprays issuing from single-hole injectors (31). The axis of the cone in which the droplets are injected is a line extending from the injector tip to the spark plug tip. Values of V_{inj}, r_{32}, and θ used in the three calculations are given in Table 6.
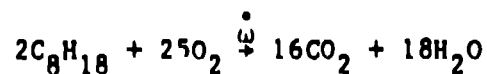
TABLE 6

SPRAY INJECTION PARAMETERS

Case	1	2	3
V_{inj} $(\frac{cm}{s})$	12,636	10,610	8,336
r_{32} (μm)	2.6	2.5	3.9
θ (degrees)	10.8	12.8	13.0

The computer model assumes a single component liquid fuel, and we use n-octane to simulate the Amoco 91 gasoline used in the experiment. The H/C ratio of n-octane is 2.25, somewhat higher than that of Amoco 91 gasoline, but the heat of reaction for the reaction of n-octane and oxygen to form carbon dioxide and water is 45.04 MJ/Kg, close to the heating value of Amoco 91.

To model ignition by the spark plug, fuel vapor and oxygen are not allowed to coexist in designated ignitor cells near the tip of the spark plug for the duration of ignition. That is, any fuel (oxygen) transported into an ignitor cell that already has oxygen (fuel), is burned. The ignitor cells are those that contain a spark plug particle from the lower 0.5 cm of the plug. Note that since the spark plug particles have fixed positions and the mesh is moving, different cells can be ignitor cells at different times.

In all cells other than ignitor cells, fuel and oxygen react chemically according to the single-step reaction

$$2C_8H_{18} + 25O_2 \overset{\dot{\omega}}{\rightarrow} 16CO_2 + 18H_2O$$

where

$$\dot{\omega} = \left[C_8H_{18}\right]^{.25}\left[O_2\right]^{1.5}c_f \ \exp(-E_f/T) \quad , \quad (7)$$

$$c_f = 1 \times 10^{11} \quad ,$$

and

$$E_f = 15780 \ K \quad .$$

The values of these adjustable reaction rate parameters are not varied for the baseline calculations reported later. As has been previously mentioned, there is much evidence that such a laminar Arrhenius rate is not appropriate for turbulent flames (29). In addition to this main fuel conversion reaction, the three kinetic reactions of the extended Zel'dovich mechanism (13) are used, and dissociation in the post-flame gases is computed by using six equilibrium reactions. The equilibrium constants for these are given in Ref. (14). Twelve chemical species are used in all calculations.

The computational time step is calculated by the code and is restricted at various times by stability and accuracy constraints associated with the calculation of convection, diffusion, and chemical reaction. Each calculation requires approximately 4600 computational cycles and three hours of computer time on a CRAY-XMP.

V.   INTERNAL OBSTACLE TREATMENT

Because of the drag exerted by the spark plug on the swirling flow and because the spark plug acts as a flame holder with combustion occurring in its wake, it is important to include the drag effects of the spark plug on the flow field in the UPS-292-SC engine. The spark plug is one example of an internal obstacle in an IC engine, other examples being fuel injectors and intake and exhaust valves. These internal obstacles have relatively complicated geometries and may move. Even if they do not move relative to the cylinder, it may be necessary to have internal obstacles move relative to a computational mesh that is

being rezoned. This is the case for the spark plug in the UP3 engine. In this section we present a method for easily incorporating the effects of internal obstacles in KIVA calculations.

Modeling internal obstacles in a fluid flow is difficult when traditional methods are used. With these methods, groups of cells, or partial volumes of cells are designated to form the obstacle. Such approaches may be used in conjunction with mesh distortions that align cell surfaces to coincide with the surface of the obstacle. Because of their complicated geometry and, possibly, their motion relative to a mesh, to represent internal obstacles by traditional methods would require a complicated, costly, and possibly time-dependent calculation of partial volumes. If mesh distortion is used, the distortions often become intolerable or are difficult to prescribe.

Our solution to this problem is to represent internal obstacles by computational particles distributed uniformly within the volume occupied by the obstacle. The position of each particle is stored in computer memory and used to locate the particle within the mesh. In addition, a radius r_{obs} is associated with the particles, where

$$\frac{4}{3} \pi r_{obs}^3 n_{obs} \sim V_{obs} \quad ,$$

The quantity n_{obs} is the number of particles used to represent the obstacle, and V_{obs} is the volume of the obstacle. In the calculations of this paper, we use $n_{obs} = 200$. We have not included the effects of the volume displaced by the obstacle, but if we had, the particle positions and volume could easily have been used to calculate the fraction of the volume of each computational cell that is occupied by the obstacle. What we have included is the effect of the drag of the obstacle on the fluid. To do this, we let each particle exert a force $\underset{\sim}{F}$ on the gas:

$$\underset{\sim}{F} = -\frac{1}{2} \rho_g |\underset{\sim}{u}| \underset{\sim}{u} \pi r_{obs}^2 c_{D,obs} \tag{8}$$

where $\underset{\sim}{u}$ is the gas velocity in the cell in which the particle is located and $c_{D,obs}$ is a constant drag coefficient. We have found that the flow through the obstacle is stopped when $c_{D,obs} = 10.0$.

The advantage of our treatment is that existing coding in KIVA for the spray particles can be used with little modification for the internal obstacle particles. This coding finds the cell in which a computational particle is located and calculates implicitly the force F exerted by the particle on the gas (14). $\tilde{}$

VI. COMPARISON OF THE EXPERIMENTAL MEASUREMENTS AND COMPUTATIONAL RESULTS

In this section we give the computed histories of several integrated quantities and compare some of these with experimental measurements. The integrated quantities are cylinder pressure, wall heat loss, chemical heat release, pressure work done on the piston, total liquid spray mass and the total masses of several gas-phase species in the cylinder. To better understand the mode of combustion, we also monitor the total mass of fuel vapor in premixed regions, which we define to be those regions in which the equivalence ratio ϕ lies between 0.5 and 3.0. Reasons are given for some of the discrepancies between the experimental and computational results.

Figures 5-7 give the computed and measured pressure histories for the three operating conditions. The largest differences between the computed and measured pressures occur near top-dead-center, and better agreement is obtained at higher load conditions. In Case 1, the computed pressure maximum is three percent too large; in Cases 2 and 3, the relative error increases to 18 and 25 percent respectively. In all three cases, the predicted maximum occurs three to four degrees earlier than the experimental maximum. The major reason for these discrepancies is that the computed heat release occurs too quickly, but because of uncertainties and inaccuracies in the submodels, it is not clear which of these submodels is responsible for the excessively fast heat release. It could be that

the chemical conversion rate of fuel is too
large, that the spray is vaporizing too fast,
that the turbulence model is mixing the fuel
and vapor too quickly, or that our computa-
tional ignition procedure is burning too much
fuel.

The experimental pressure curves from
Cases 2 and 3 also exhibit some interesting
behavior not seen in the calculated curves.
During fuel injection the rate of pressure
rise drops slightly and immediately after in-
jection, but still during ignition, the rate
of rise increases. A possible explanation for
this is that during injection the chemical
heat release is small and the rate of pressure
rise drops because the upward motion of the
piston is slowing. Then after injection there
is a large increase in the rate of chemical
heat release.

Smaller differences in the pressure
curves are discernable before injection and
after 30° ATDC. Before injection the computed
pressures are slightly higher. To investigate
the cause of these early pressure differences
we recalculate Case 3, suppressing ignition
and combustion. In one calculation the spray
is allowed to vaporize at its normal rate; in
a second calculation we evaporate the spray
droplets as soon as they are injected. The
idea is to assess how combustion and spray
evaporation alter the computed pressure histo-
ry. The results are shown in Fig. 8. It is
seen that spray evaporation has little effect
on the computed pressures. At 5° BTDC the
computed pressure without combustion is 9%
larger than the experimental value. About
half of this difference is accounted for by a
difference in compression ratios. For our
computational mesh the compression ratio is
13.44, three percent higher than the true com-
pression ratio of 13.0. To see how this ef-
fects the pressure, we observe first that near
top-dead-center the ratio of our calculated
combustion chamber volume V_{calc} to the experi-
mental volume V_{exp} is the ratio of compression
ratios:

$$\frac{V_{calc}}{V_{exp}} = \frac{13.0}{13.44} = 0.967 \quad .$$

Assuming approximately isentropic pressure changes and an average value of the ratio of specific heats $\gamma = 1.35$, gives

$$\frac{p_{calc}}{p_{exp}} = \left(\frac{V_{exp}}{V_{calc}}\right)^{\gamma} = 1.046 \quad .$$

The remaining part of the difference at 5° BTDC between the experimental pressure and that calculated without combustion, could be because the calculations underpredict the wall heat loss. The additional pressure change needed to give agreement is approximately $1.0 \times 10^6 \frac{dynes}{cm^2}$. With the average density $\bar{\rho}$ at 5° BTDC equal to 1.33×10^{-2} g/cm^3 and the average molecular weight $\bar{W}$ approximately that of N_2, we find that an average temperature drop δT of about 25 K would make calculation and experiment agree:

$$\delta T = \frac{\delta p \, \bar{W}}{\bar{\rho} \, R} = \frac{(1 \times 10^6)(28)}{(1.33 \times 10^{-2})(8.31 \times 10^7)} = 25 \text{ K} \quad .$$

Since the specific heat of N_2 at constant volume and 800 K is about $8.5 \times 10^6 \frac{erg}{g - K}$ and since there are 0.84 grams of gas in the cylinder, a temperature drop of 25 K would be brought about by an additional energy loss of 1.8×10^8 ergs, which is about 70% of the wall heat loss at 5° BTDC in the calculations without combustion. As we shall see from the comparison of experimental and calculated total wall heat losses, it is conceivable that there is a 70% error in our calculated wall heat loss at 5° BTDC.

Thus by using the correct compression ratio of 13.0 and by increasing our calculated wall heat losses by 70%, agreement would be obtained between the experimental pressure at 5° BTDC and the calculated pressure without combustion. This is direct support for our earlier observation that there is an ignition delay in Cases 2 and 3. If there is additional combustion in Case 3 before 5° BTDC, additional wall heat losses would be needed to

bring calculation and experiment into agreement. While a 70% error in our computed wall heat loss is conceivable a much higher error is not likely based on the errors in our total wall heat losses.

After 30° ATDC, the computed pressures in Figs. 5-7 are again higher. In addition to errors in the computed wall heat loss and compression ratio, errors in the total heat release from chemical reactions probably contributed to the discrepancies after 30° ATDC. The latter errors become larger with decreasing load.

That the computed wall heat loss is too low can be seen in Figs. 9-11. These figures give the computed histories of the chemical heat release from all chemical reactions (WCHEM), the heat lost to the cylinder walls (WHEAT, and the pressure work done by the gas on the linder (WPDV). Significant wall heat loss begins approximately when chemical heat release becomes significant. In all three calculations the computed rate of wall heat loss reaches a maximum between 10° and 20° ATDC and thereafter diminishes. At 90° ATDC, the computed wall heat loss is approximately 65% of the experimentally reported value for all calculations. Since the experimental measurement is based on exhaust gas temperature and exhaust valve opening occurs at approximately 118° ATDC, it would be better to use computed wall heat losses at 118° ATDC for comparison. From the slopes of the curves in Figs. 9-11, however, there will be very little additional wall heat loss between 90° and 118° ATDC. Thus, the calculations uniformly underpredict the experimental wall heat loss by approximately 50% of the calculated values.

Based on the heat release plots of Figs. 9-11, the computed combustion efficiency increases with decreasing load, and this is opposite the trend observed in the experiments. In Case 3, chemical heat release is nearly complete at 40° ATDC. In Case 2, this does not occur until approximately 80° ATDC and in Case 1 exothermic chemical reaction is still occurring at 90° ATDC. Noted in each figure is the theoretical maximum heat release if all fuel were oxidized to water and carbon dioxide. The difference between this value and the plateau in the WCHEM curve for Case 3, is attributable to dissociation of the burn products.

That the computed combustion efficiency
increases with decreasing load is also shown
in the plots of Figs. 12-14, which give the
total liquid fuel mass and fuel vapor mass
versus crank angle. In Case 1, 2.6% of the
injected fuel remains unburned at 90° ATDC,
whereas in Cases 2 and 3 this same figure is
0.2% and 0.0%. One can also see from Figs.
12-14 that the spray vaporizes more rapidly in
Cases 2 and 3 than in Case 1.

In Figs. 12-14, there are sudden jumps in
the curves of liquid fuel and fuel vapor mass.
This occurs when there is rapid vaporization
of a computational spray particle that has a
large mass associated with it. These massive
particles are present because of the method
used to calculate spray droplet coalescence
(14). To test if any significant numerical
errors are associated with having massive par-
ticles, we calculate Case 1 again using a
method for splitting massive spray particles
into smaller ones. By increasing the number
of computational particles that represent the
spray, the particle splitting procedure im-
proves the accuracy of the spray calculation.
Figure 15 compares the fuel liquid and vapor
mass curves for the calculations with and
without particle splitting. It is seen that
the curves with particle splitting are
smoother, and that with splitting the liquid
vaporizes more slowly. There are not signifi-
cant differences between the pressure curves
for the two calculations.

It is of interest to know whether the
fuel is consumed by premixed or diffusion
flames, and for this reason we monitor the
total mass of fuel vapor in premixed regions.
We define premixed cells to be those in which
the equivalence ratio ϕ lies between 0.5 and
3.0. From these curves, which are plotted in
Fig. 16, we can see when the premixed burn
phase is complete. In Case 1 this occurs ap-
proximately at top-dead-center, and in Cases 2
and 3 premixed burning is complete at 7° ATDC.
For Cases 2 and 3 we also monitor the total
mass of fuel burned in these premixed regions.
In both cases this is about six percent of the
total fuel mass injected. Thus only a small
fraction of the fuel is burned by premixed
flames.

Figures 17-19 give the computed total masses of NO, CO, and CO_2 in the cylinder.

The predicted NO mass agrees well with measured NO_x mass in Cases 1 and 3 and is 37% low in Case 2. In all three calculations the NO is produced between 10° BTDC and 30° ATDC, when the gases in the cylinder are hottest due to compression and combustion. After 30° ATDC, cooling of the expanding gases causes the NO-producing reactions of the Zel'dovich mechanism to freeze.

In all calculations there is poor agreement between predicted and measured CO and CO_2 concentrations. This is to be expected for two reasons. First we have used a single step chemical reaction to model the complex fuel oxidation kinetics. Second, a significant fraction of the carbon atoms in the engine are involved in soot formation and combustion, a phenomenon that is not presently included in our model.

VII. PARAMETER VARIATIONS

In this section we report the results of calculations to test the sensitivity of the pressure to some of the computational and physical parameters. All calculations are of Case 3, in which the poorest agreement with experiment was obtained. The parameters we vary are the reaction rate, the initial spray droplet sizes and velocities, the size of the ignition region, and the ignition timing. Reducing the size of the ignition region by a factor of two, reduces the computed pressure very little. A similar effect on the pressure is obtained when we delay ignition by 7.5° to begin at 10° BTDC. The most sensitivity is displayed when the reaction rates and spray injection parameters are varied, and we focus our discussion on these below. We did not vary any parameters associated with the k-ε model for turbulent mixing; it is expected that the computed pressures would also have been sensitive to these.

Figure 20 shows the effects of varying the reaction rate factor c_f on the computed pressure history. Doubling c_f changes the

pressures very little, but lowering c_f by factors of two and ten results in dramatically lower pressures. In the calculation with $c_f = 1 \times 10^{10}$, complete flame extinction occurs and very little of the fuel is burned. It is likely that good agreement between measured and calculated pressures can be obtained using a value of c_f between 1×10^{10} and 5×10^{10}. The insensitivity of the results to increasing c_f above 1×10^{11} may be due to the structure of the flames in our calculation. Because of the reaction rate Eq. (7) that we have used the calculated turbulent flames have the structure of laminar flames, except they are thicker. Since most of the burning in the calculation is by diffusion flames and since the rate of reactant consumption in laminar diffusion flames depends primarily on the diffusivities of mass and energy and not the reaction rate, we might expect the computed pressures to be insensitive to increases in c_f above some value for which flame extinction does not occur

The results are also very sensitive to variations in the spray injection parameters. In one calculation we raise the injection velocity by a factor of 1.5 and lower the mean drop size by a factor of 2.25. In a second calculation we raise the mean drop size to $10 \ \mu m$ and keep the injection velocity the same as in the baseline calculation. As shown in Fig. 21, with increasing drop size the pressure is reduced. This is a reasonable consequence of the fact that larger drops vaporize more slowly, but other output diagnostics reveal a slightly more complicated picture. In the largest drop-size case, the drops vaporize more slowly, but this effect is partially negated by enhanced penetration of the spray, which exposes the drops to more hot gas without vapor. At $2°$ ATDC, when we terminate the calculation, the amount of fuel burned in premixed regions is nearly the same as in the baseline calculation. If we had continued the calculation, however, combustion would have been far different than in the baseline calculation because spray particle plots reveal that a large fraction of the drops have impinged on the wall of the piston bowl.

In the smallest drop size calculation
spray penetration is nearly the same as in the
baseline calculation. The smaller drops are
more tightly coupled to the gas flow, an ef-
fect that inhibits penetration, but this ef-
fect is apparently offset by the higher injec-
tion velocity we used. Thus, vaporization
rates are enhanced both by the smaller drop
sizes and the higher injection velocity. Cor-
respondingly, the amount of fuel burned in
premixed regions is 45% higher than in the
baseline calculation. Interestingly, when the
calculation terminates at 20° ATDC, the mass
of NO is 50% higher than the baseline calcu-
lation value, because combustion has produced
more hot gas sooner.

VIII. AN EXAMINATION OF THE DETAILED FLOW
     FIELDS CALCULATED FOR CASE 1

In this section we examine computer-
generated plots from Case 1 of the velocity
fields, the spray particle positions, and con-
tours of selected scalar variables. The com-
puted pressures of Case 1 agree closely with
experiment, and hence the total chemical heat
release versus time is close to that of the
experiment. Because of this agreement the
plots we will describe are a reasonable guess
for the flow fields in the UPS-292-SC engine
under the higher load conditions of Case 1.
Using this guess, we gain qualitative insight
into the fluid dynamics, spray, mixing, and
combustion in the engine.

A challenging aspect of three-dimensional
calculations lies in visualizing the complex
flow fields and in relating the different flow
field properties to determine the causes of
the observed flow features. In this section
we present two-dimensional velocity vector
plots and contour plots of scalar variables in
selected planes that slice through the three-
dimensional flow field. The velocity vector
plots show the projections of the velocity
vectors onto the selected planes. By juxta-
posing several such plots one gains a reasona-
ble comprehension of the three-dimensional
flow field at a given time. We have also made
a movie that shows the temporal evolution of
some of the velocity vectors and contour plots
in four selected planes. We describe the

movie and use several frames from it to point
out interesting flow features in the engine.

The velocity vectors at 58° BTDC shown in
Fig. 22 are characteristic of those observed
during compression and before combustion,
although the squish velocities do become more
pronounced as top-dead-center is approached.
The integers j and k are the azimuthal and
axial indices of computational cells. Thus
the plot identified as "j=1 and 10" gives the
velocity vectors of those cells whose azimuth-
al indices are one and ten. The position of
this plane is shown in the plot associated
with k equal 22. It is seen that the j-equal-
1-and-10 plane slices through the center of
the spark plug. The plots show how the swirl-
ing flow is diverted around the spark plug.
That flow diverted inward accelerates because
of the need to conserve angular momentum. The
k-equal-12 plane shows a dead region in the
spark plug scallop. The k-equal-22 and k-
equal-12 planes show that the center of rota-
tion of the fluid does not coincide with the
axis of the cylinder and that the center of
rotation varies with axial position. During
the calculation the center of rotation proc-
esses but remains within two radial cell di-
mensions of the cylinder axis. A very per-
sistent feature of the flow field prior to
combustion is the vortex observed in the wake
of the spark plug in the j-equal-16 plane. A
possible explanation for this vortex is that
since the rotating fluid accelerates as it is
diverted inward around the spark plug, by
Bernoulli's Law its pressure drops. Thus, the
flow near the cylinder head behind the plug is
pulled radially inward.

Turbulence levels are important to engine
designers because higher turbulence levels
lead to enhanced combustion rates. Figure 23
gives contour plots of the specific turbulent
kinetic energies at 58° BTDC in the j-equal-1-
and-10 and j-equal-7-and-16 planes. Generally
these are lowest near the walls of the chamber
and higher in the interior. The highest
levels are observed in the wake of the spark
plug. Another local maximum lies near the
spark plug scallop.

One would expect the swirl velocities to
deflect the spray radially inward, but very
little of this effect is seen in the spray

particle position plots of Fig. 24 at 13°
BTDC, or at any other time. Shown here are
the positions of all spray particles, pro-
jected onto the viewing planes. It could be
that the small drops vaporize quickly, leaving
large drops that are not very tightly coupled
to the swirling flow. The plots of Fig. 24 do
show that the spray is very thin and collim-
ated, despite the fact that the initial spray-
cone angle is 10.8°. To check that we were
indeed injecting particles in a 10.8° cone, we
recalculated Case 1 beginning at injection and
using very large drops that had straight-line
trajectories. The large particle positions
did fall exactly within a 10.8° cone. Thus
the narrowing of the spray for the smaller
drops of Case 1 is due to the drag exerted on
the spray by the gas flow. Because the spray
is injected cocurrently with the flow and
because the swirl velocities are approximately
two-thirds the injection velocity, the drops
are deflected inward toward the axis of the
spray cone.

Figure 25 shows plots of the velocity
vectors and contours of turbulent kinetic en-
ergy and length scale in the j-equal-1-and-10
and j-equal-7-and-16 planes at 13° BTDC. The
velocity vectors show the flow out of the
squish region. They also show combustion-
induced velocities near the spark plug in the
j-equal-1 plane and in the wake of the plug in
the j-equal-7 plane. The turbulence field has
changed from that seen in Fig. 23, but the
change is perhaps not what one would expect.
Because of velocity shears induced by the
squish flow, one might guess that the highest
turbulence intensities would be observed near
the rim of the piston bowl. The plots show
however that the highest intensities are lo-
cated in the interior of the piston bowl.
This is because the dissipation rate of turbu-
lent kinetic energy $\epsilon \sim k^{3/2}/L$, where L is the
length scale, and L is very small near walls,
as shown in Fig. 25. Hence ϵ is large near
walls and smallest in the interior of the
piston bowl.

We now present several frames from the
computer-generated movie depicting the flow
field of Case 1. The movie has two segments;
the first shows contour plots of equivalence

ratio and temperature as in Fig. 26, and the
second shows the velocity field as in Fig. 27.
In both segments views of four planes are
shown: the j-equal-1-and-10 plane and three
k-planes. As shown in Figs. 26 and 27 a line
is drawn from each k-plane to its axial loca-
tion on the j-equal-1-and-10 plane. The white
contour line of Fig. 26 is associated with an
equivalence ratio of one; the fuel-rich vapor
cloud lies in the interior of this contour.
In the movie three other contours are drawn.
These are isotherms associated with tempera-
tures of 1700 K, 2000 K, and 2300 K and are
drawn with the colors green, yellow, and red,
respectively. These are not shown in the
black and white plots of Fig. 26. Constant
scaling factors are used to determine the
lengths of the velocity vectors. One value is
used for the j-plane, and a smaller value is
used for the k-planes because the velocities
in these planes are approximately a factor of
two larger.

In the contour plots of Fig. 26 at $7°$
BTDC, the high temperature region lies only on
one side of the fuel cloud. This is during
the premixed burn phase of the combustion, and
a flame is at this time consuming premixed
fuel that lies in a region where the equiva-
lence ratio ϕ nearly equals one. By watching
the movement of the isotherms in the movie,
the viewer will see the progress of the pre-
mixed flame as it burns the near-stoichio-
metric mixture at the periphery of the fuel
cloud. At top-dead-center the premixed burn
is complete, and the fuel cloud is surrounded
by hot combustion gases produced by the pre-
mixed burn. After top-dead-center all burning
is by diffusion flames, which are located at
the position of the $\phi=1$ contour line. Figure
28 shows a frame of the contour plot movie at
$9°$ ATDC, during the diffusion-flame phase.
The fuel cloud and diffusion flames are being
convected around the combustion chamber and
into the squish region by the mean gas motion.

Generally the swirling gas motions are
seen in the k-plane velocity vector plots, and
the combustion- and squish-induced velocities
are seen in the j-plane plots. At $7°$ BTDC in
Fig. 27 there is a maximum in the swirl veloc-
ities near the rim of the piston bowl. This
is caused by the convection of gas with high
angular momentum out of the squish region. At
$7°$ BTDC the premixed flame has arrived at the

j-plane 180° opposite the spark plug. This is
evidenced by the divergence of velocity vec-
tors located in this j-plane. Later, as shown
by the velocity vectors of Fig. 29 at 9° ATDC,
the gas flows out of the combustion chamber
and into the squish region. The maximum in
the swirl velocities at the piston bowl rim
disappears, and a minimum in the swirl veloc-
ities appears in the squish region. This is
the wake of the spark plug, which as been con-
vected into the squish region.

IX. CONCLUSION

A three-dimensional numerical model has
been used to simulate the spray, mixing, and
combustion in the UPS-292-SC engine. The re-
sults of the calculations greatly modify and
supplement previous hypotheses for the events
occurring in the engine. It is found that be-
cause of the high swirl 'locities and co-
current spray injection, the spray is colli-
mated and thereby, evaporation is inhibited.
The combustion occurs in two phases: a short
premixed burn during which a small fraction of
the fuel is consumed, followed by a longer
diffusion flame phase. The flames are not
stationary but are convected around the com-
bustion chamber and into the squish region by
the gas flow.

Concerning the numerical model the calcu-
lations show that when used in conjunction
with experimental measurements, KIVA can give
useful qualitative insights into the three-
dimensional spray dynamics, mixing, and com-
bustion in internal combustion engines. The
ability of the model to predict pressure his-
tories and pollutant emissions is limited by
inaccurate submodels for some of the control-
ling physical processes. Predicted qualita-
tive trends must be evaluated in light of
these inaccuracies.

REFERENCES

1.   F. V. Bracco, "Introducing a New Genera-
      tion of More Detailed and Informative
      Combustion Models," SAE Trans. Vol. 84,
      p. 3317 (1975).

2.   F. V. Bracco, "Modeling of Two-Phase,
      Two-Dimensional Unsteady Combustion for
      Internal Combustion Engines," Stratified
      Charge Engines, I. Mech. E. Conference
      Publications 1976-11, p. 167 (1976).

3. R. B. Krieger, "Applications of Engine
    Combustion Models," Combustion Modeling
    in Reciprocating Engines, eds.
    J. N. Mattavi and C. A. Amann (Plenum
    Press, New York 1980), p. 485.

4. F. V. Bracco and P. J. O'Rourke, Prog.
    Energy Combust. Sci. 7, 103 (1981).

5. T. D. Butler, L. D. Cloutman,
    J. K. Dukowicz, and J. D. Ramshaw, Prog.
    Energy Combust. Sci. 7 293 (1981).

6. A. D. Gosman, "Aspects of the Simulation
    of Combustion in Reciprocating Engines,"
    Numerical Simulation of Combustion
    Phenomena, eds. R. Glowinski,
    B. Larrouturou, and R. Temam (Springer-
    Verlag, Berlin, 1985), p. 46.

7. T. D. Butler and P. J. O'Rourke, "A
    Numerical Method for Two-Dimensional
    Unsteady Reacting Flows, Sixteenth
    Symposium (International) on Combustion
    (Combustion Institute, Pittsburgh, 1976),
    p. 1503.

8. P. J. O'Rourke, and F. V. Bracco,
    J. Comput. Phys. 33, 185 (1979).

9. J. Abraham, F. V. Bracco, and
    R. D. Reitz, Combustion and Flame 60, 309
    (1985).

10. A. D. Gosman and P. S. Harvey, "Computer
    Analysis of Fuel-Air Mixing and Combus-
    tion in an Axisymmetric D. I. Diesel
    Engine," SAE paper 820036 (1982).

11. A. D. Gosman, Y. Y. Tsui, and
    A. P. Watkins, "Calculation of Three-
    Dimensional Air Motion in Model Engines,"
    SAE paper 840229 (1984).

12. H. Shappertons and F. Thiele, "Three-
    Dimensional Computations for Flow Fields
    in DI Piston Bowls," SAE paper 860463
    (1986).

13. F. A. Williams, "Combustion Theory,"
    (Benjamin/Commings Publishing Company,
    Inc., Menlo Park, CA, 1985), p. 446.

14. A. A. Amsden, J. D. Ramshaw,
P. J. O'Rourke, and J. K. Dukowicz,
"KIVA: A Computer Program for Two- and
Three-Dimensional Fluid Flows with
Chemical Reactions and Fuel Sprays,
Los Alamos National Laboratory report
LA-10245-MS (1985).

15. A. A. Amsden, J. D. Ramshaw,
L. D. Cloutman, and P. J. O'Rourke,
"Improvements and Extensions to the KIVA
Computer Program," Los Alamos National
Laboratory report LA-10534-MS (1985).

16. K. Meintjes and A. P. Morgan,
"Equilibrium Equations for a Model of
Combustion," General Motors Research
Laboratories report GMR-4361 (1983).

17. J. D. Ramshaw and A. A. Amsden,
J. Comput. Phys. 59, 3, 484 (1985).

18. J. K. Dukowicz, J. Comput. Phys. 35, 229
(1980).

19. J. M. Lewis and W. T. Tierney, "United
Parcel Service Applies Texaco Stratified
Charge Engine Technology to Power Parcel
Delivery Vans-Progress Report," SAE paper
801429 (1981).

20. J. M. Lewis and T. K. McBride, "UPS
Multifuel Stratified Charge Engine
Development - Progress Report," SAE paper
831782 (1983).

21. J. M. Lewis, "UPS Multifuel Stratified
Charge Engine Development Program - Field
Test," SAE paper 860067 (1986).

22. E. G. Groff, private communication.

23. A. A. Amsden, T. D. Butler,
P. J. O'Rourke, and J. D. Ramshaw, "KIVA:
A Comprehensive Model for 2D and 3D
Engine Simulations," SAE paper 850554
(1985).

24. P. J. O'Rourke, "The KIVA Computer
Program for Multidimensional Chemically
Reactive Fluid Flows with Fuel Sprays,"
Numerical Simulation of Combustion
Phenomena, eds. R. Glowinski,
B. Larrouturou, and R. Temam (Springer-
Verlag, Berlin, 1985), p. 74.

25. L. C. Haselman, "TDC -- A Computer Code
    for Calculating Chemically Reacting
    Hydrodynamic Flows in Two Dimensions,"
    Lawrence Livermore Laboratory report
    UCRL-52931 (1980).

26. J. R. Bakke and B. H. Hjertager, "The
    Effect of Explosion Venting in Empty
    Vessels," Proc. Fourth Int. Conf. on
    Numerical Methods in Thermal Problems,
    Swansea, 1985.

27. K. N. C. Bray, P. A. Libby, and
    J. B. Moss, Comb. and Flame 61, 87
    (1985).

28. M. M. Gibson, Int. J. Heat Mass Transfer
    21, 1609 (1978).

29. P. A. Libby and F. A. Williams, "Funda-
    mental Aspects," Turbulent Reacting
    Flows, Topics in Applied Physics Vol. 44,
    eds. P. A. Libby and F. A. Williams,
    (Springer-Verlag, Berlin 1980), p. 1.

30. A. U. Chatwani and F. V. Bracco, "Compu-
    tations of Dense Spray Jets," Proc. Int.
    Conf. Liquid Atomization and Spray
    Systems, 1985.

31. P. J. O'Rourke and F. V. Bracco,
    "Modeling of Drop Interactions in Thick
    Sprays and a Comparison with Experi-
    ments," Institution of Mechanical
    Engineers Publication 1980-9, 1980.

32. R. D. Reitz and F. V. Bracco, Phys.
    Fluids 25, 10, 1730 (1982).

33. R. D. Reitz and R. Diwalker, "Structure
    of High Pressure Fuel Sprays," submitted
    to the SAE Congress and Exposition,
    February 1987.

34. S. Wahiduzzaman and C. R. Ferguson,
    "Convective Heat Transfer from a Decaying
    Swirling Flow Within a Cylinder," Eighth
    Intern. Heat Transfer Conf., Paper
    #86-IHTC-253, August 1986.

UPS ENGINE COMBUSTION CHAMBER

Los Alamos

Fig 1.

Fig. 2 ... Department of Energy, Conserv ...
... and Combustion ... Distribution (Columbia ...)
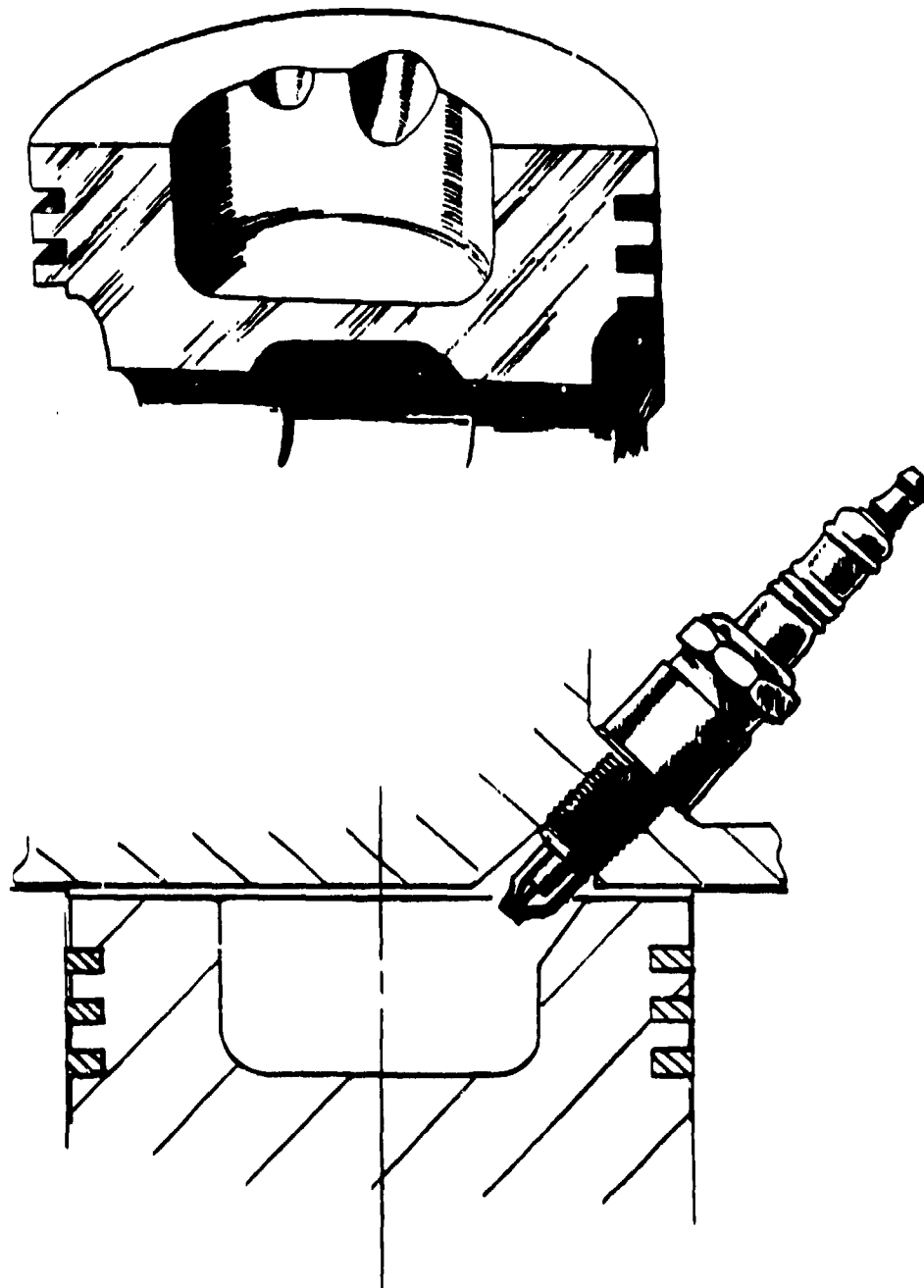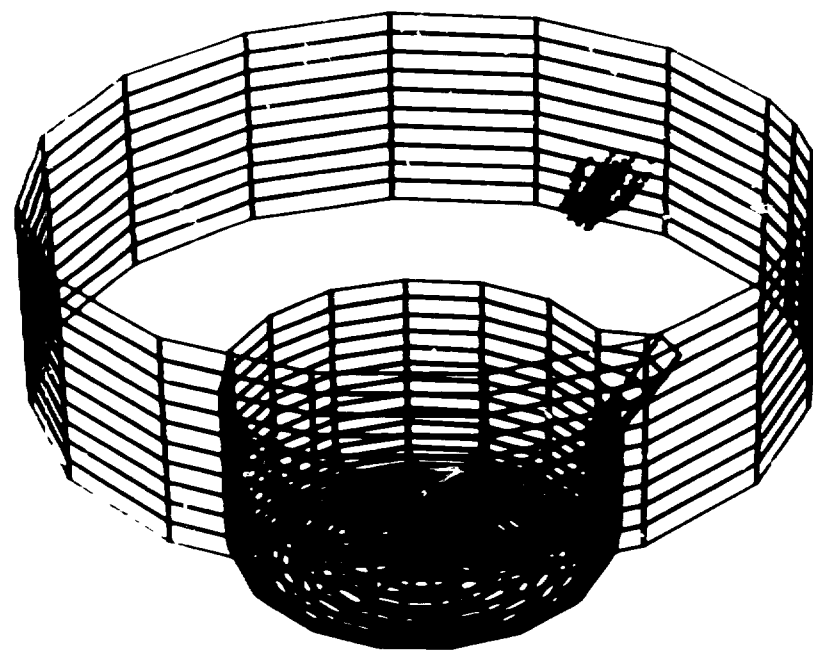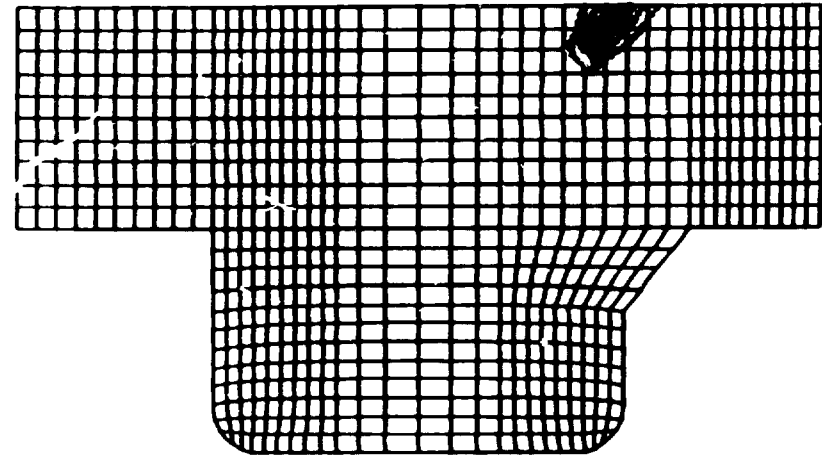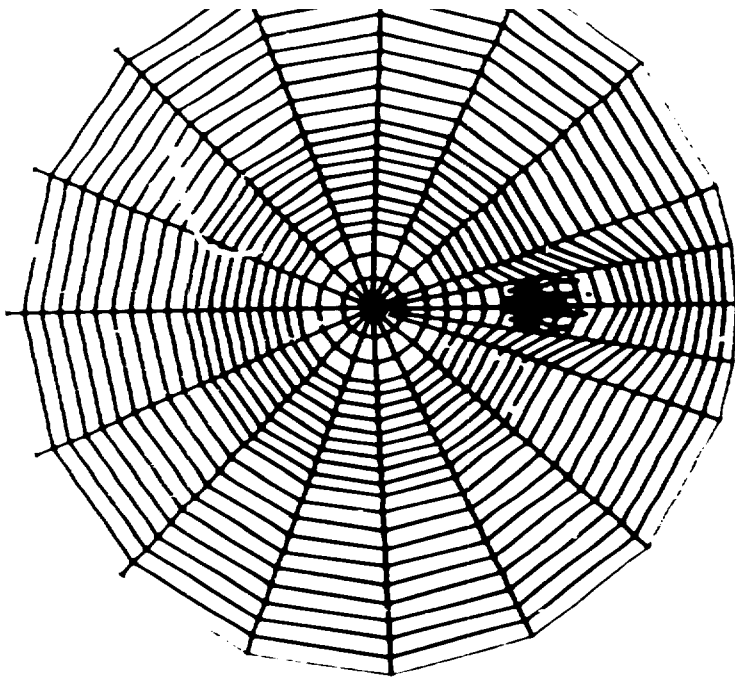
Fig. 3 Top, side, and perspective views of the KIVA computational mesh at 35° BTDC.
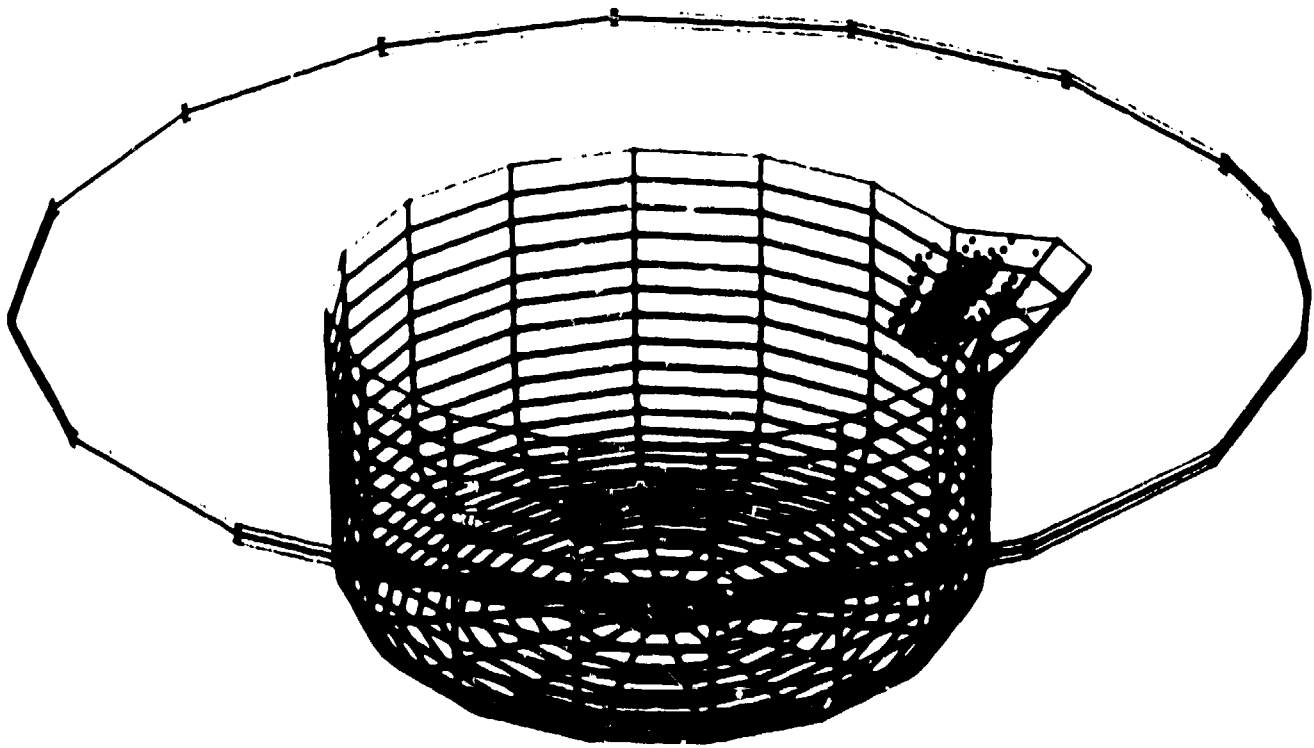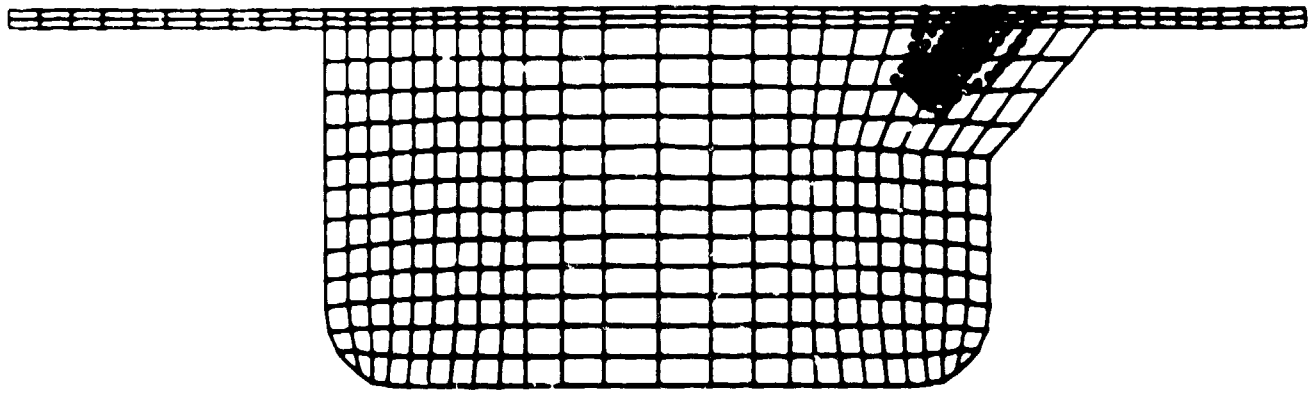
Fig. 4   Side and perspective views of the KLM4 computational mesh for 2° ATBC.
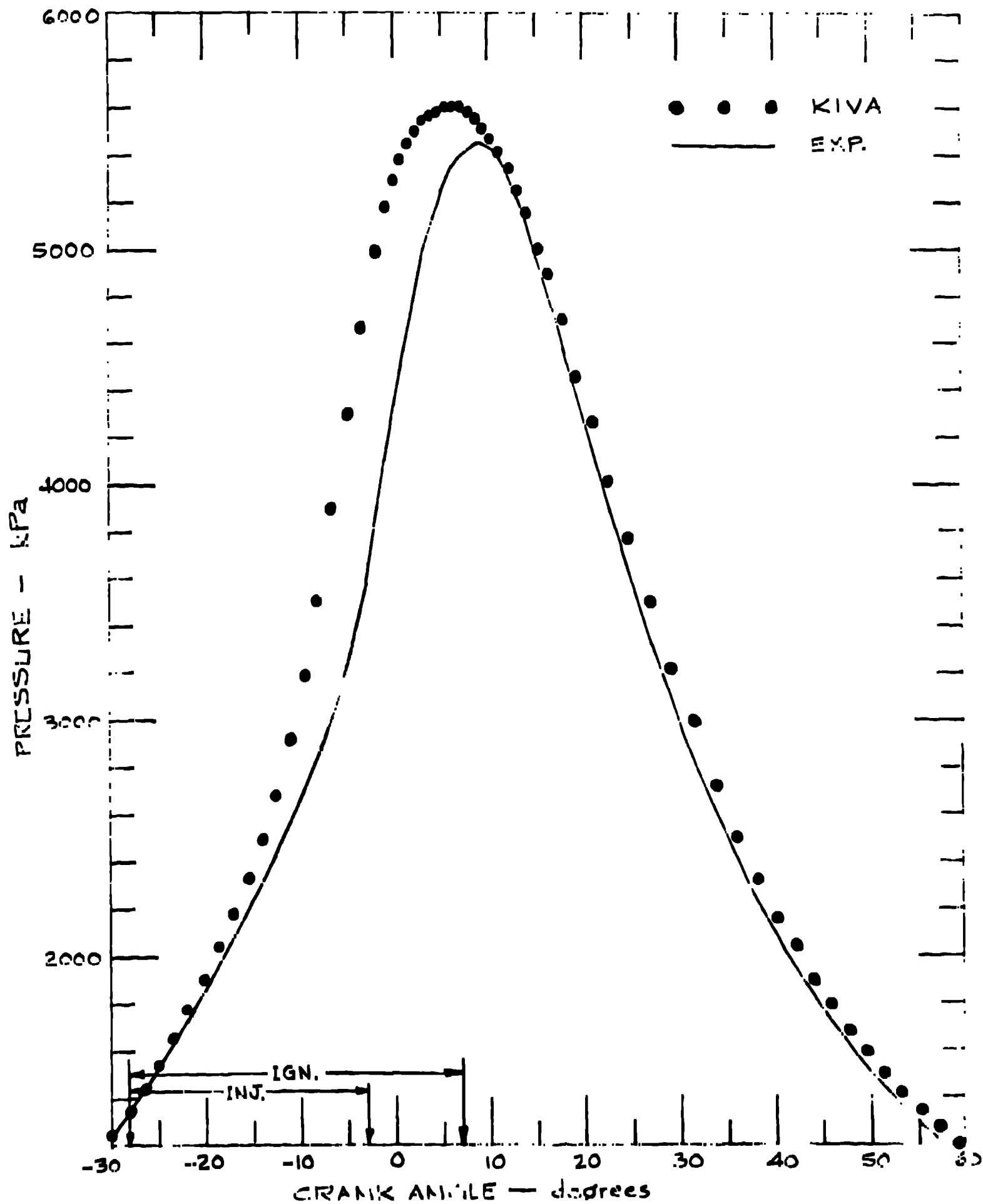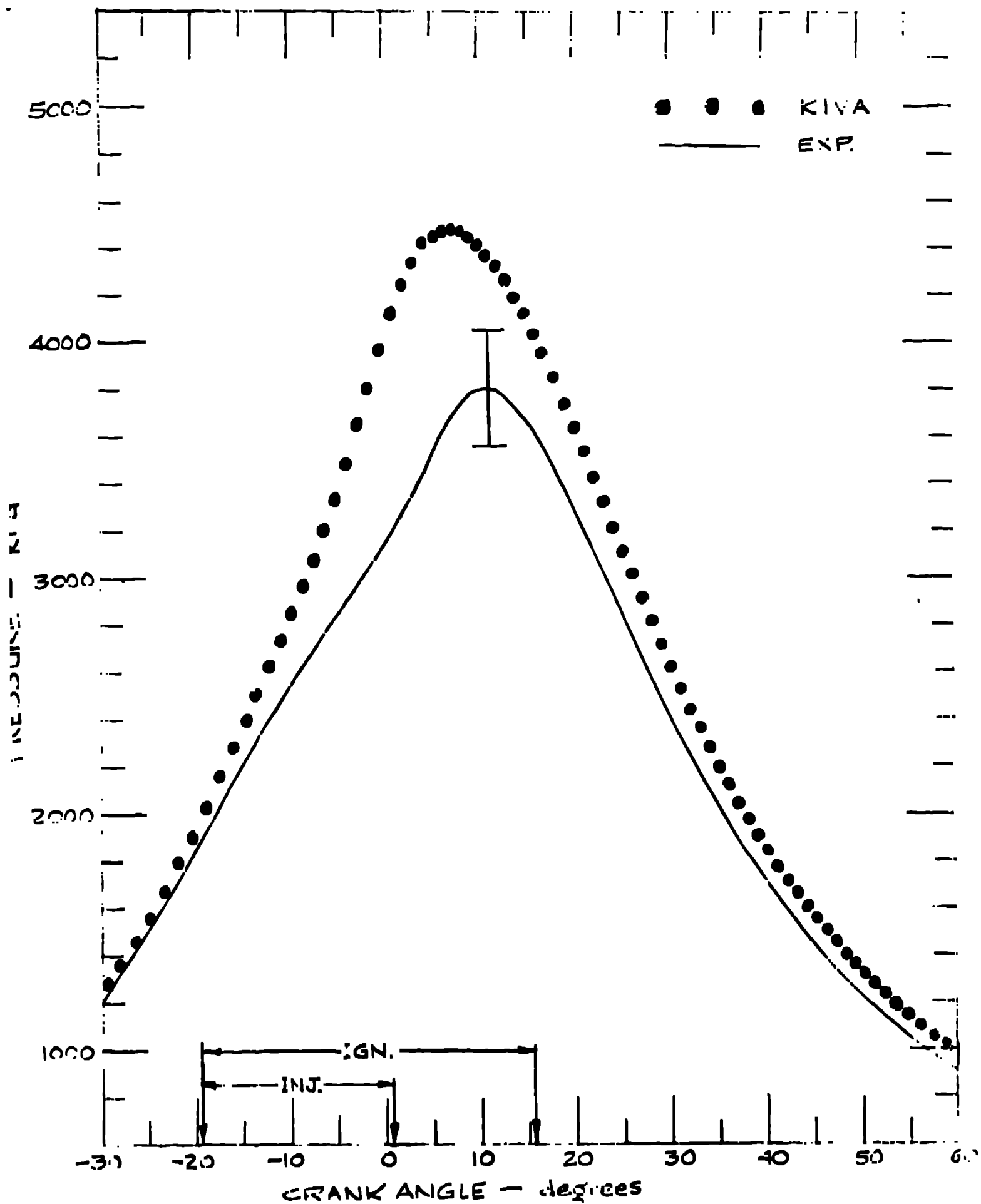
CASE 1

CASE 2

CASE 3

KIVA • • • •
EXP. ⎯⎯⎯

5000

4000

3000

2000

1000

IGN.
INJ.

-30   -20   -10   0   10   20   30   40   50

CRANK ANGLE — degrees

CASE 3

CASE 2

Fig. 11

CASE 3

Fig. 13.

CASE 2

20.8 mg INJECTED

TOTAL FUEL MASS
INJECTED

PARTICLE MASS
+ VAPOR MASS

PARTICLE
MASS

VAPOR
MASS

IGN.

INJ.

FUEL — mg

CRANK ANGLE — degrees

Fig. 14

CASE 3

FUEL — mg

CRANK ANGLE -- degrees

12.3mg INJECTED

TOTAL FUEL MASS INJECTED

PARTICLE MASS + VAPOR MASS

VAPOR MASS

PARTICLE MASS

IGN.

INJ.

Fig. 4.3

CASE 1

Fig. 16

CASE 1

CASE 2

CASE 3

MASS — $gms \times 10^4$

CRANK ANGLE — degrees
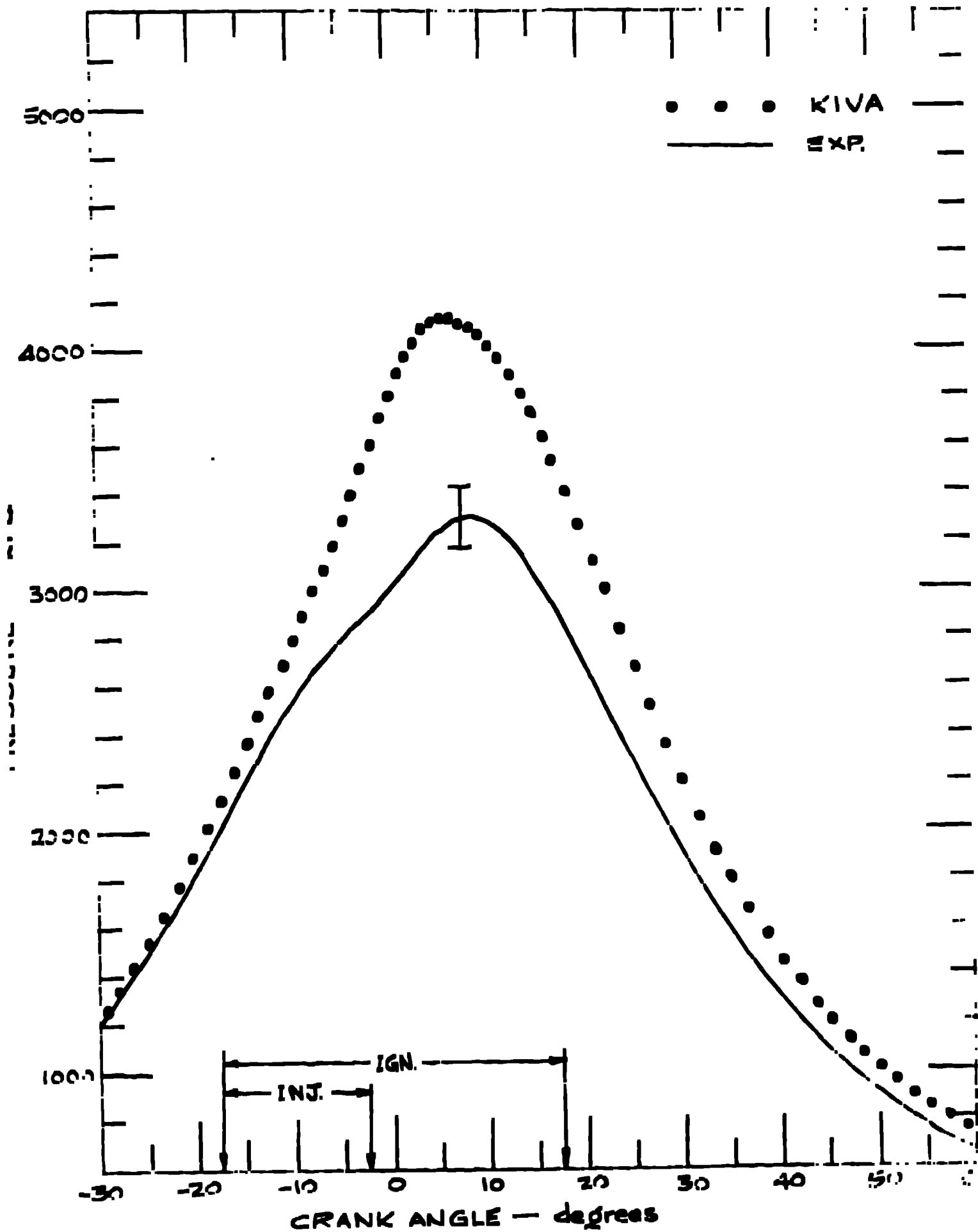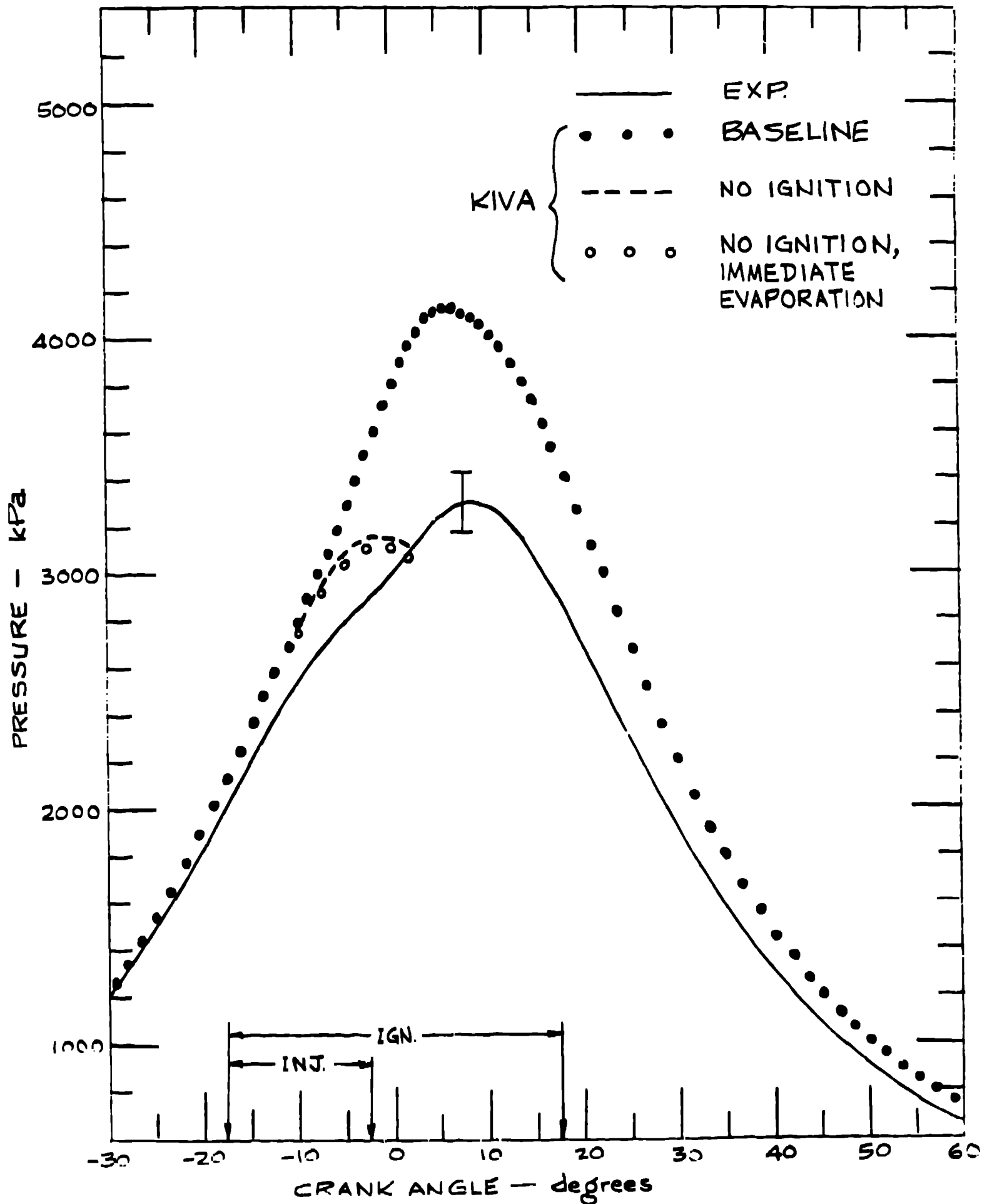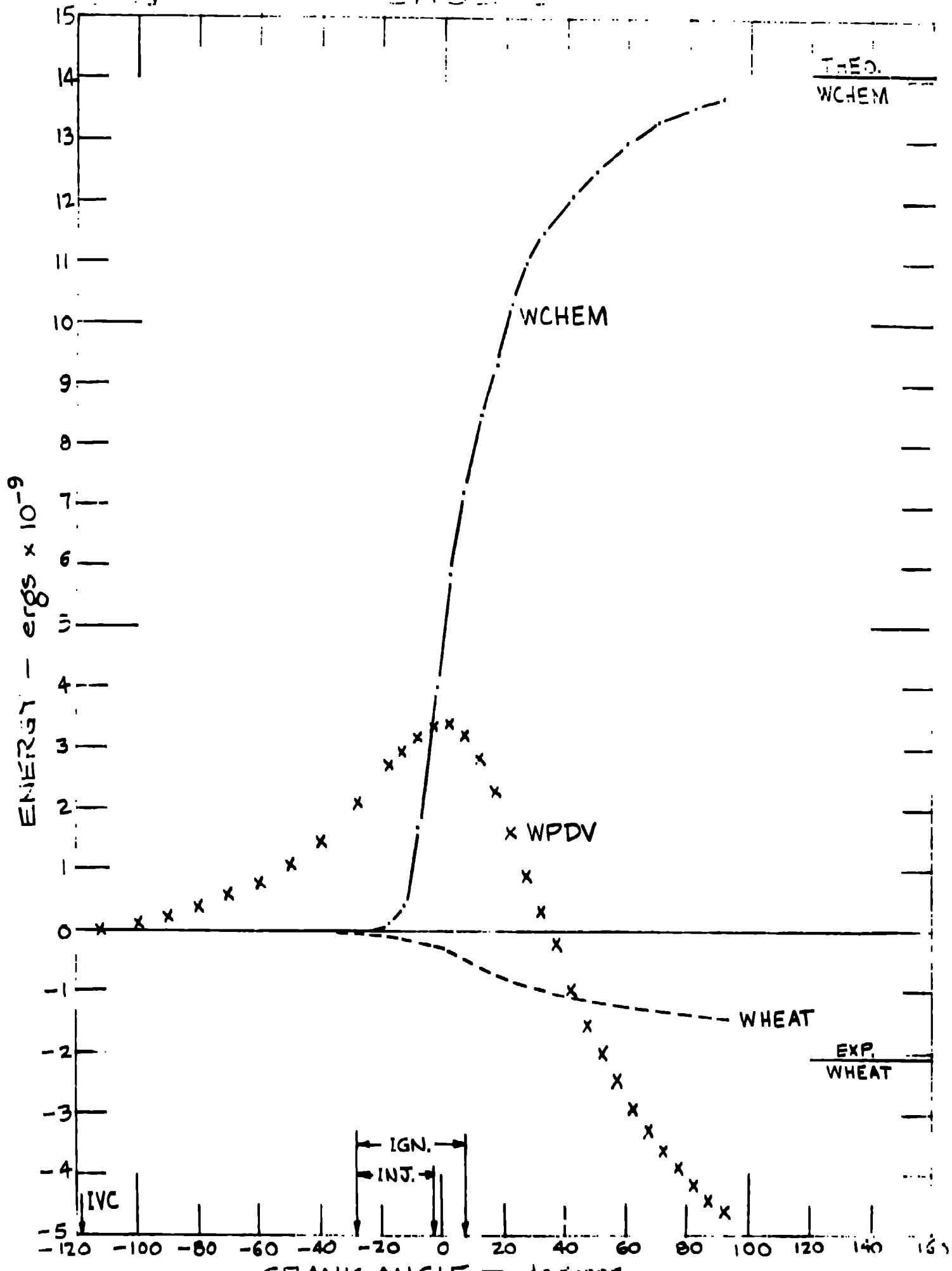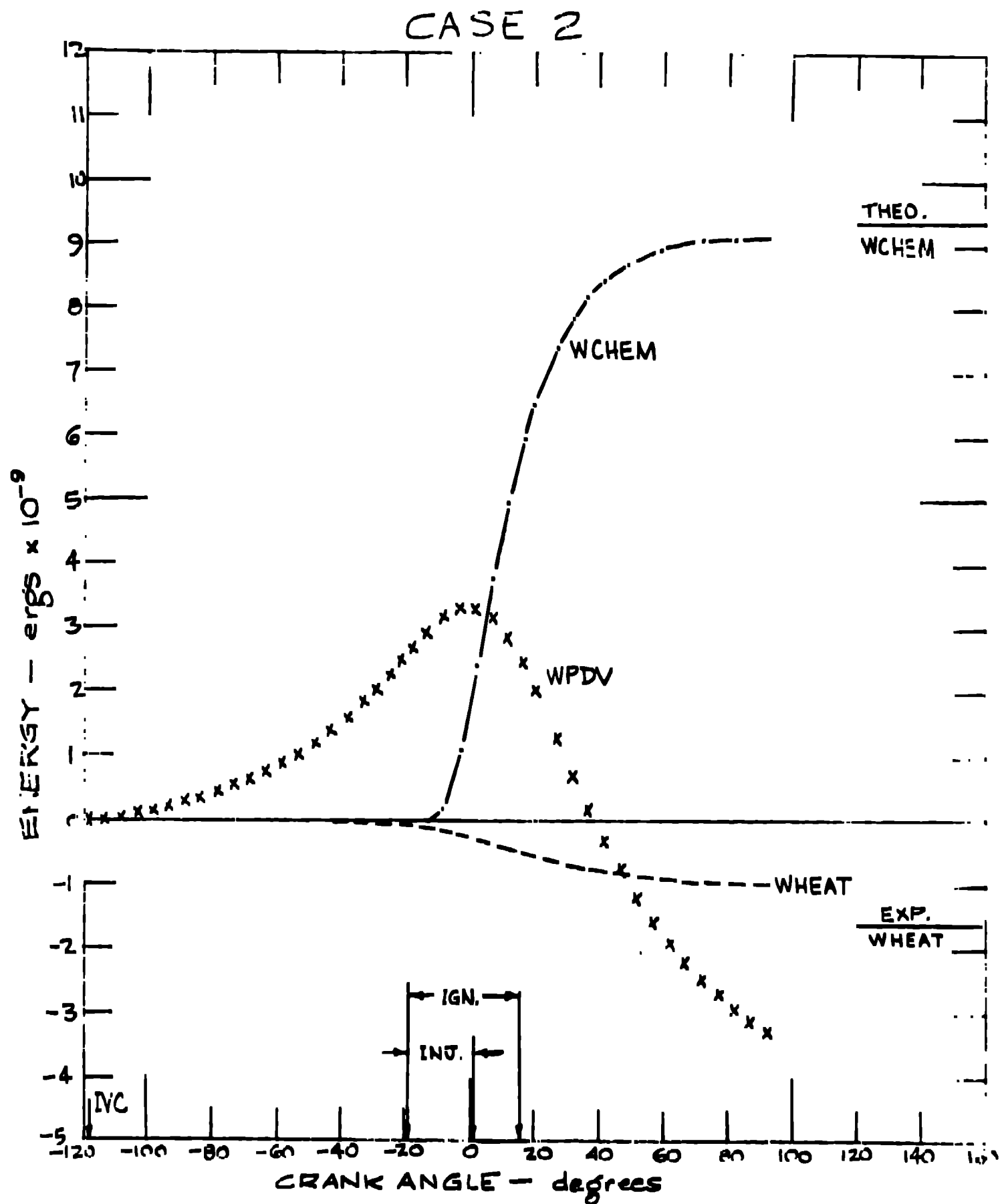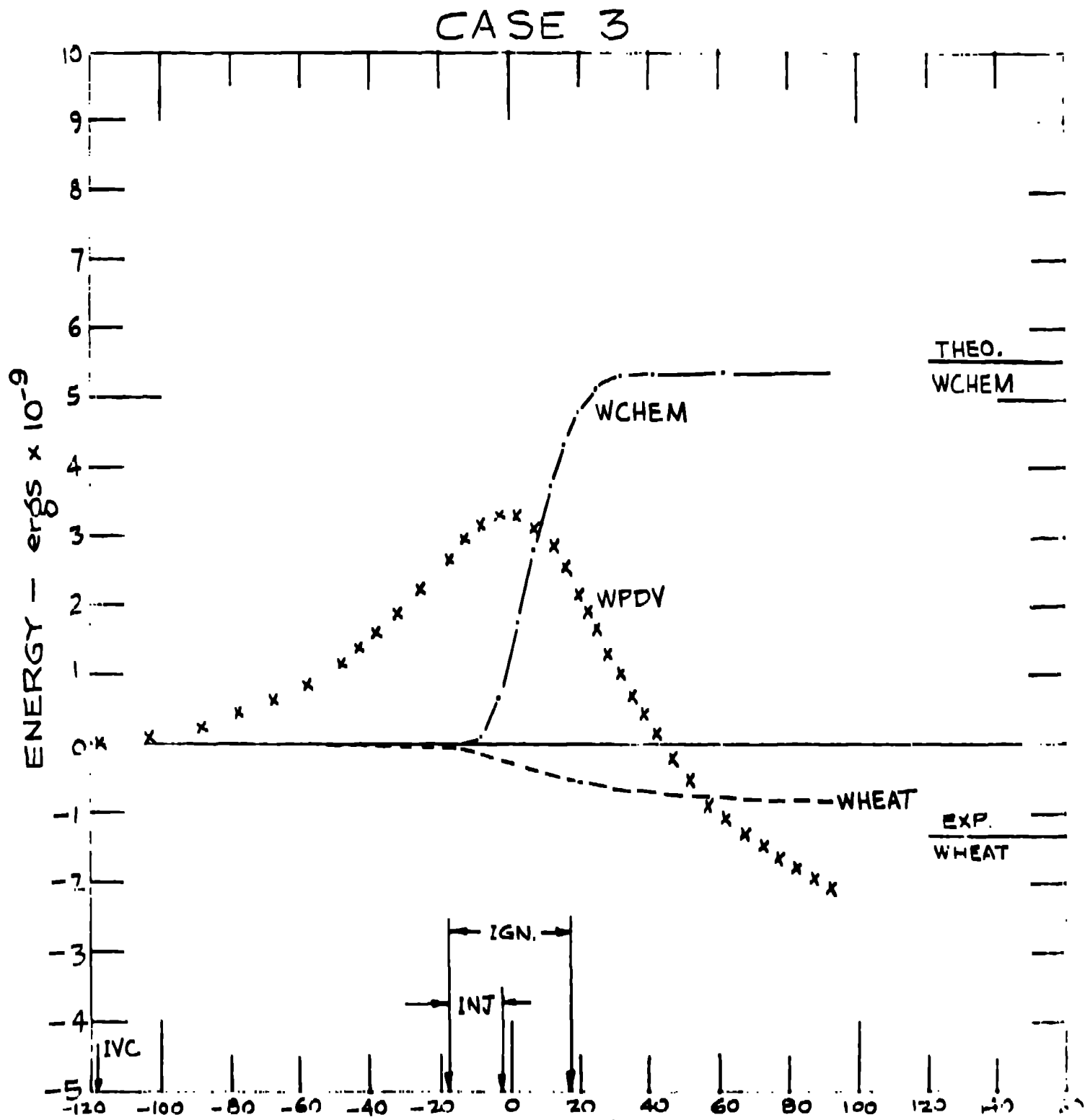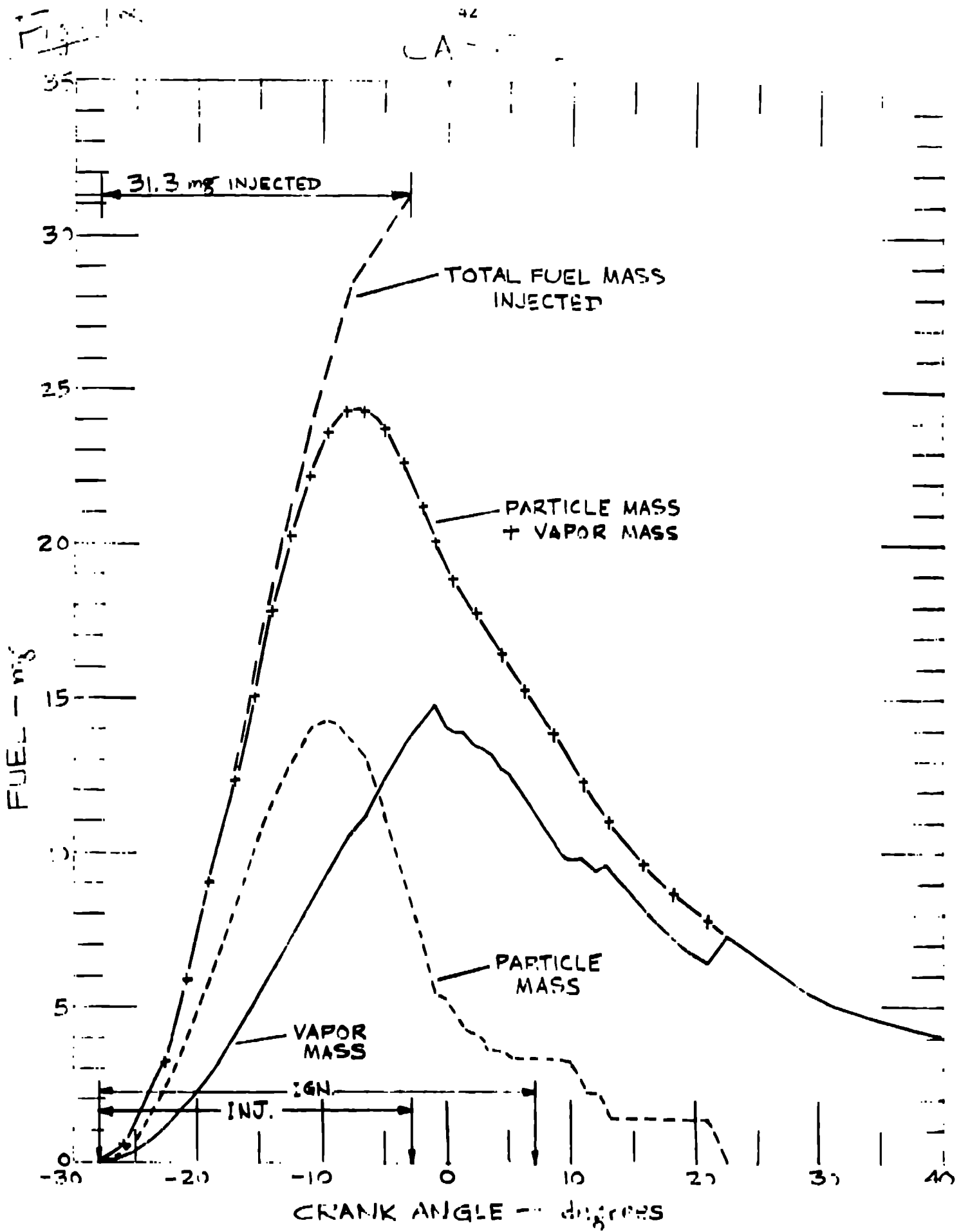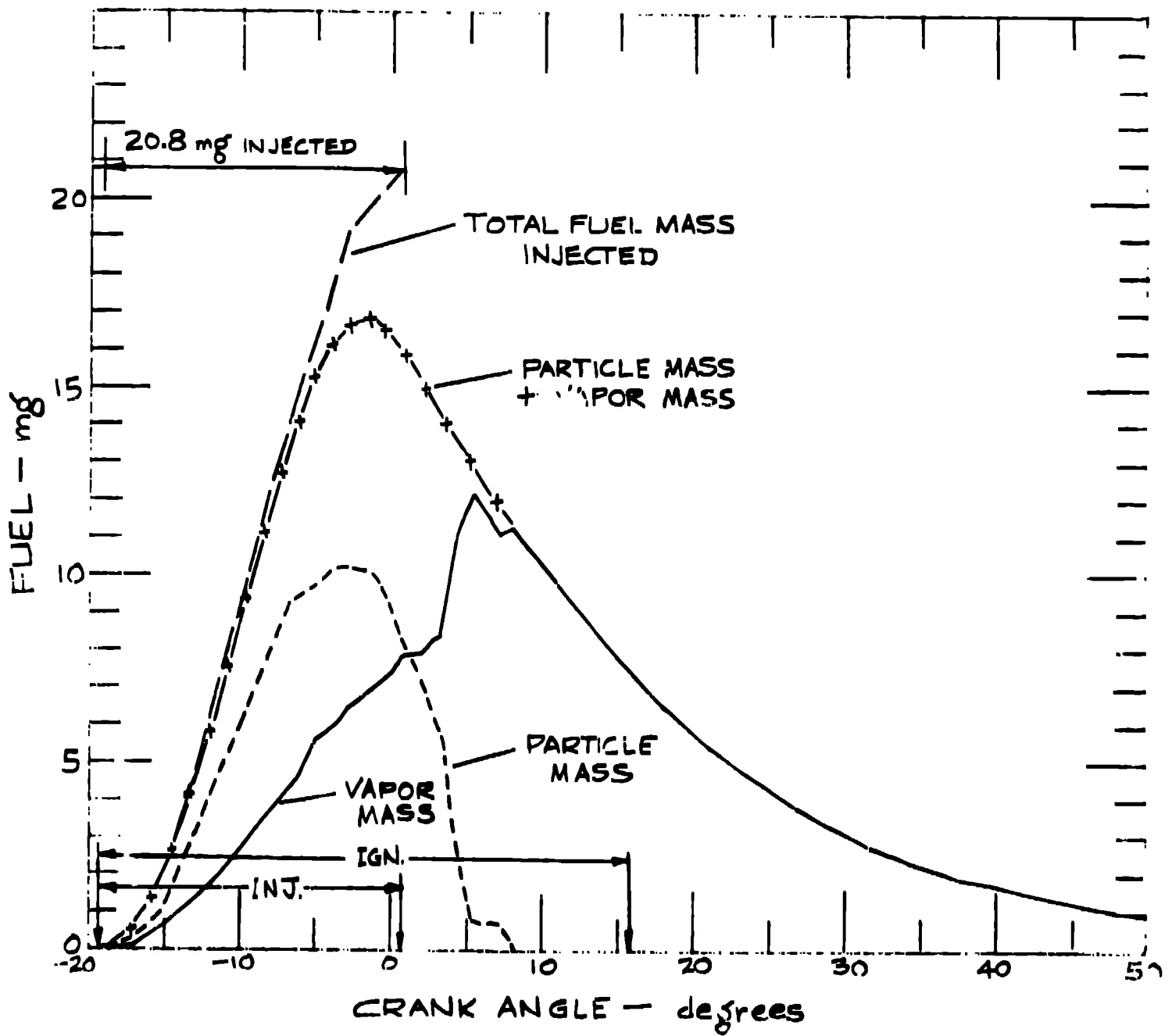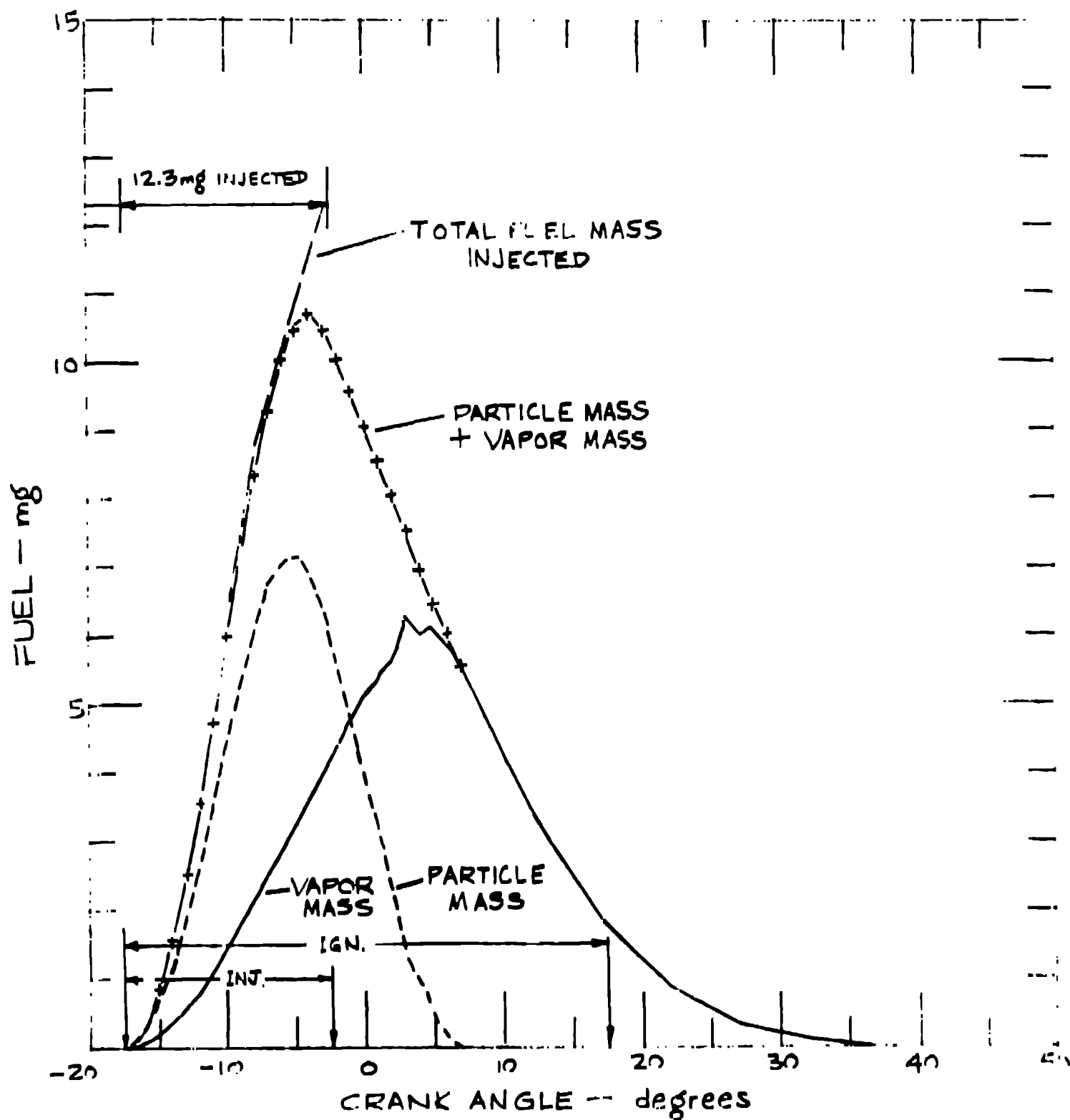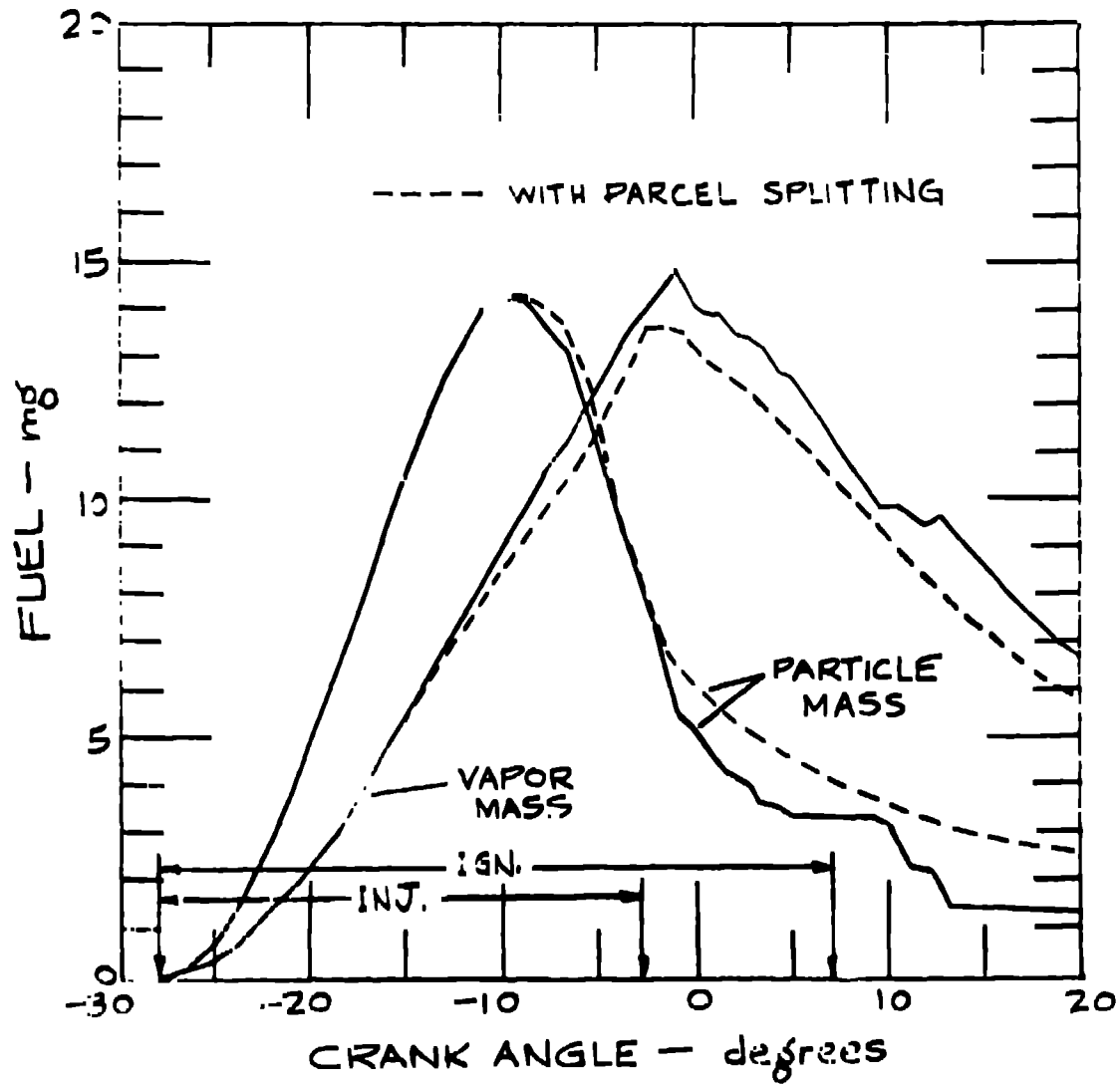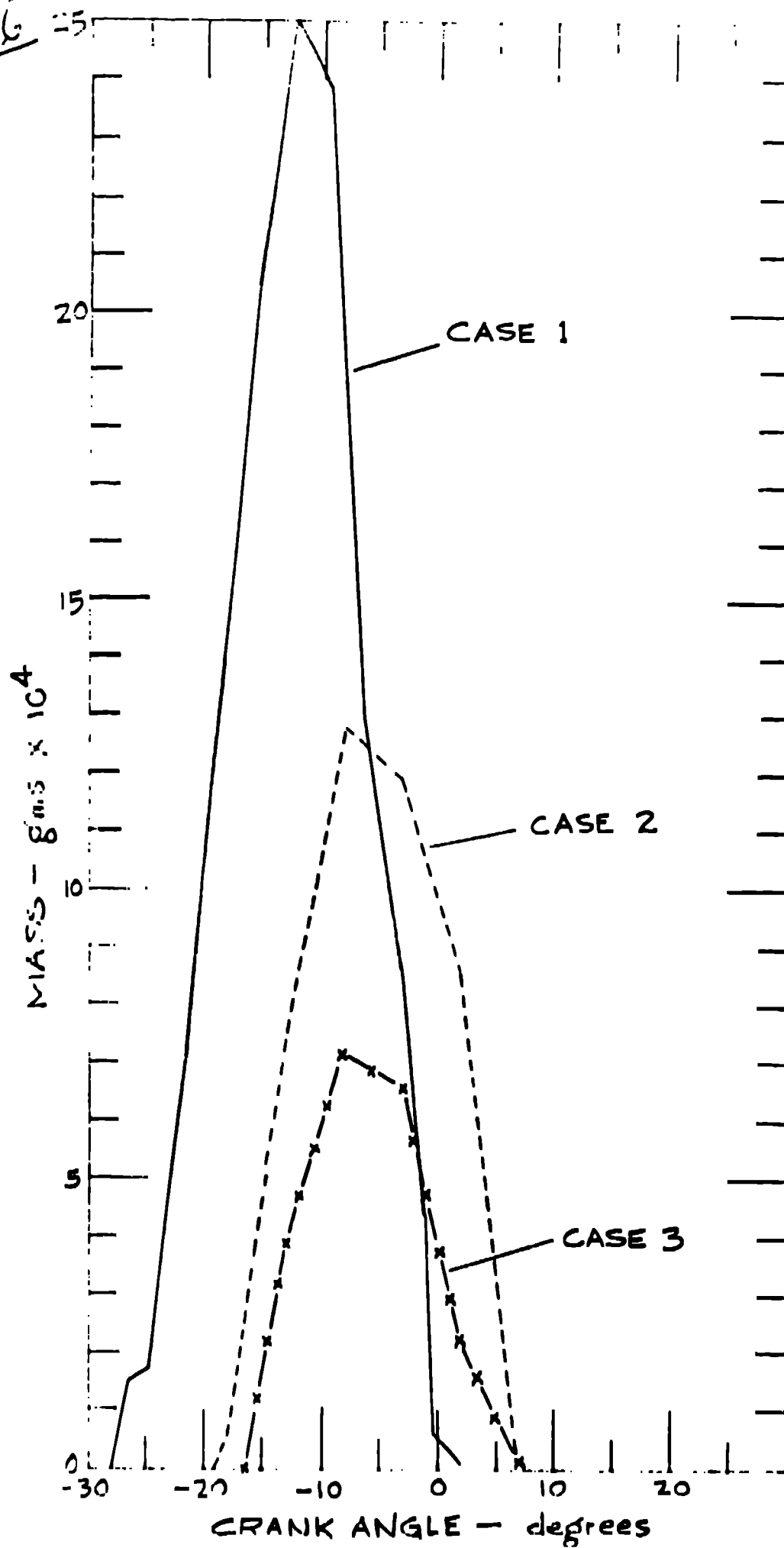
Fig.17

CASE 1

Fig. 18

CASE 2

CRANK ANGLE — degrees
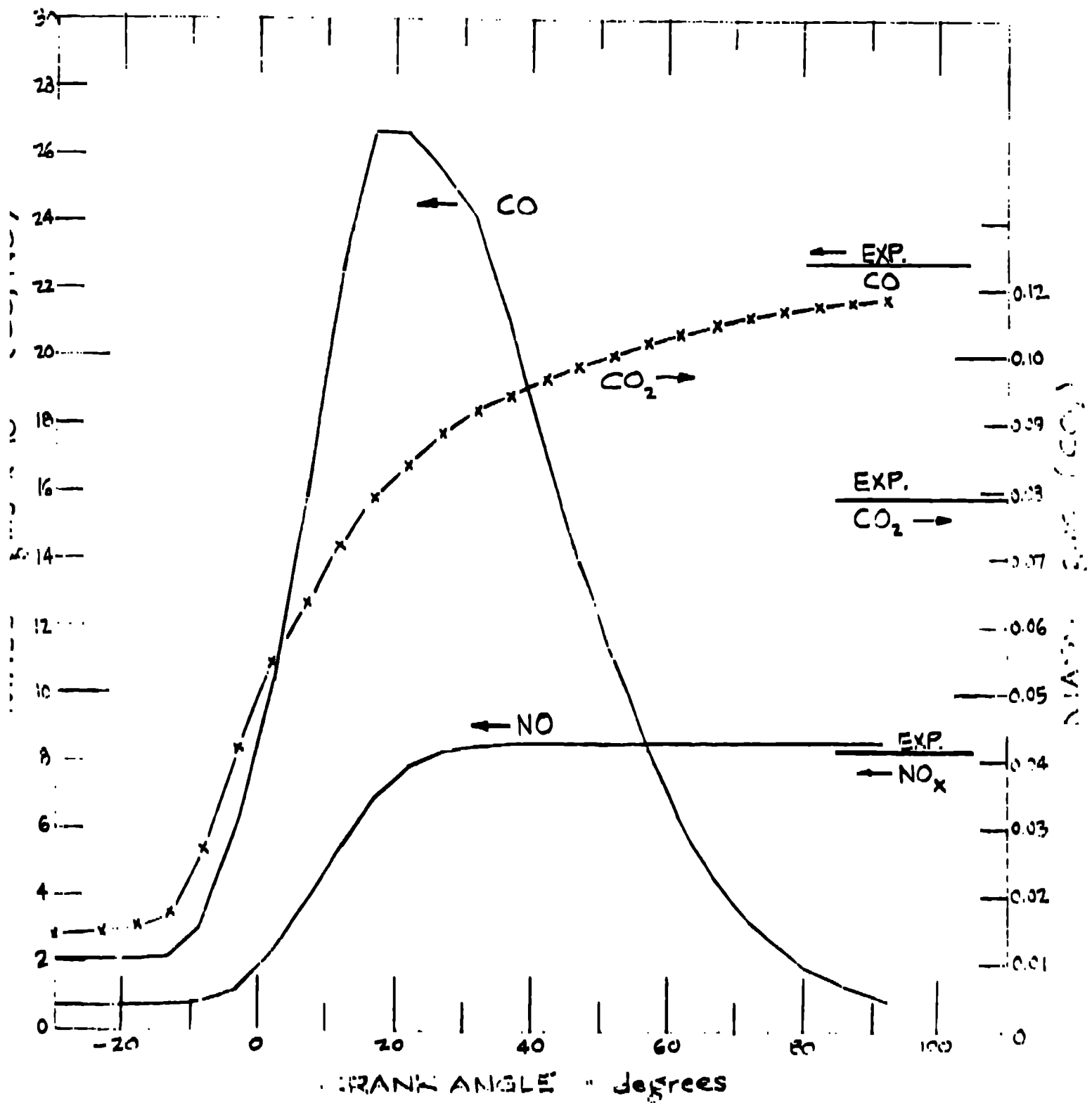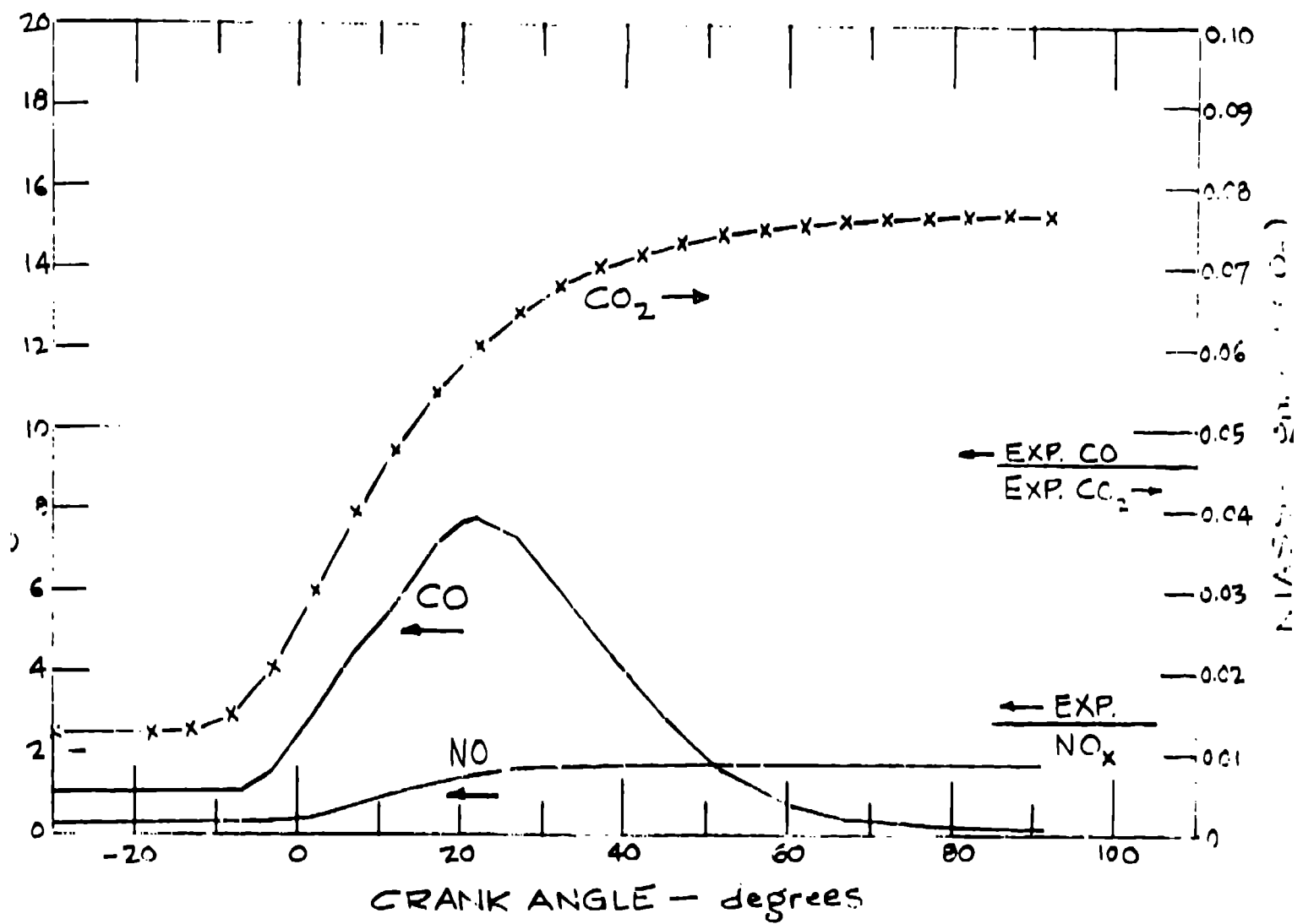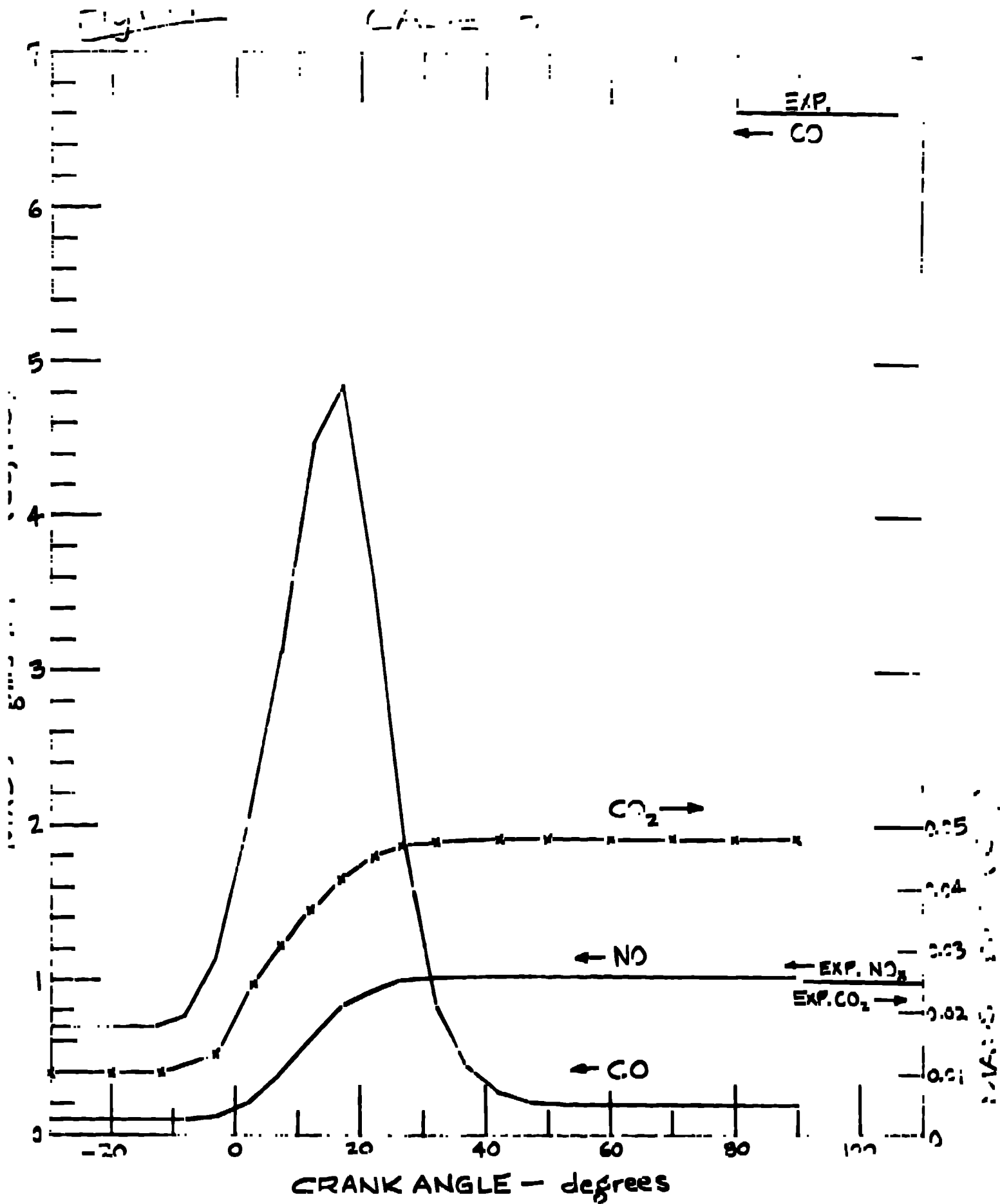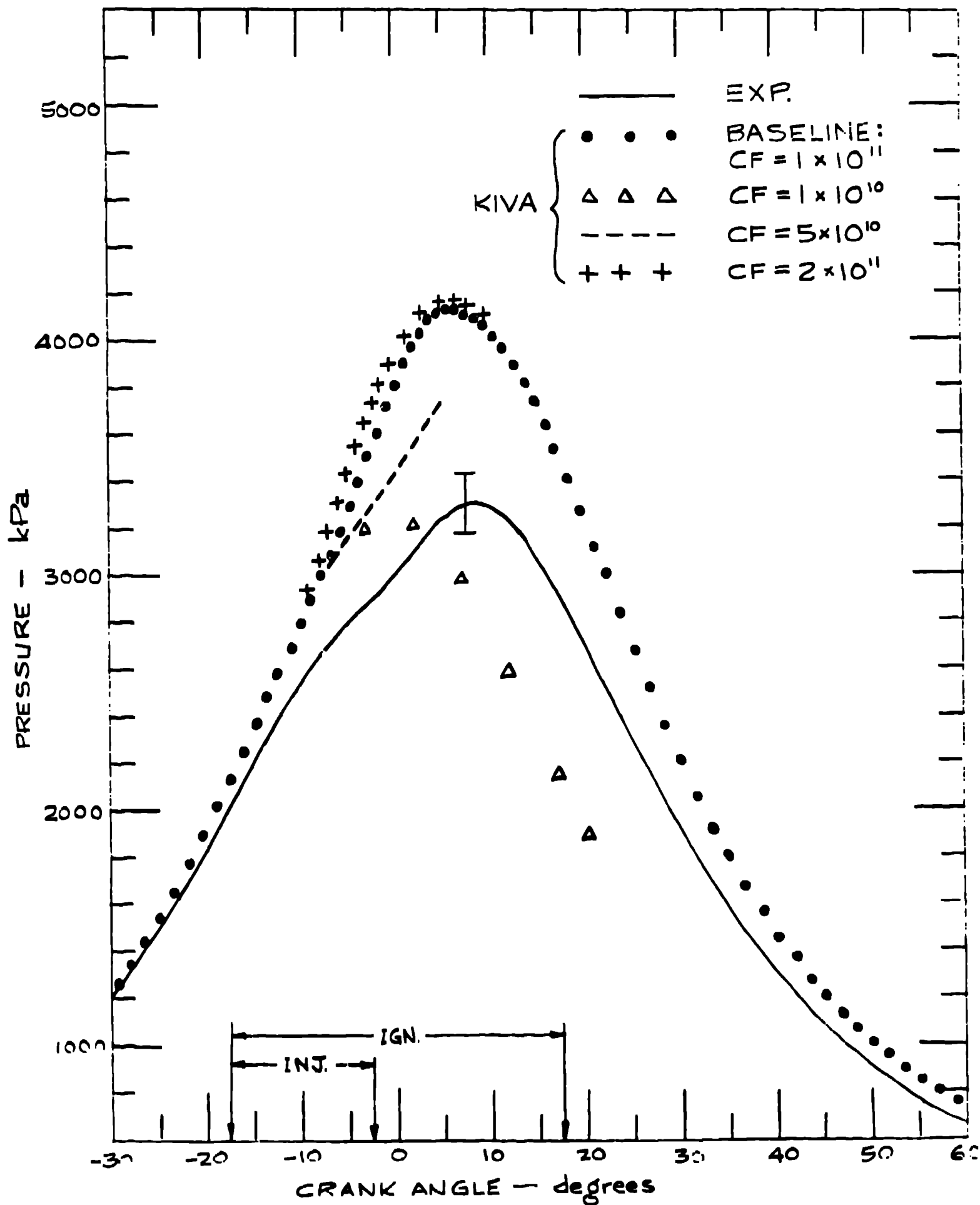
CASE 3

CASE 3

VELOCITIES AT 58° BTDC

k = 22

j = 1 & 10: u_{max} = 1824 cm/sec

j = 10

j = 1

k = 22: u_{max} = 5460 cm/sec

k = 12

j = 7 & 16: u_{max} = 2285 cm/sec

j = 7

j = 16
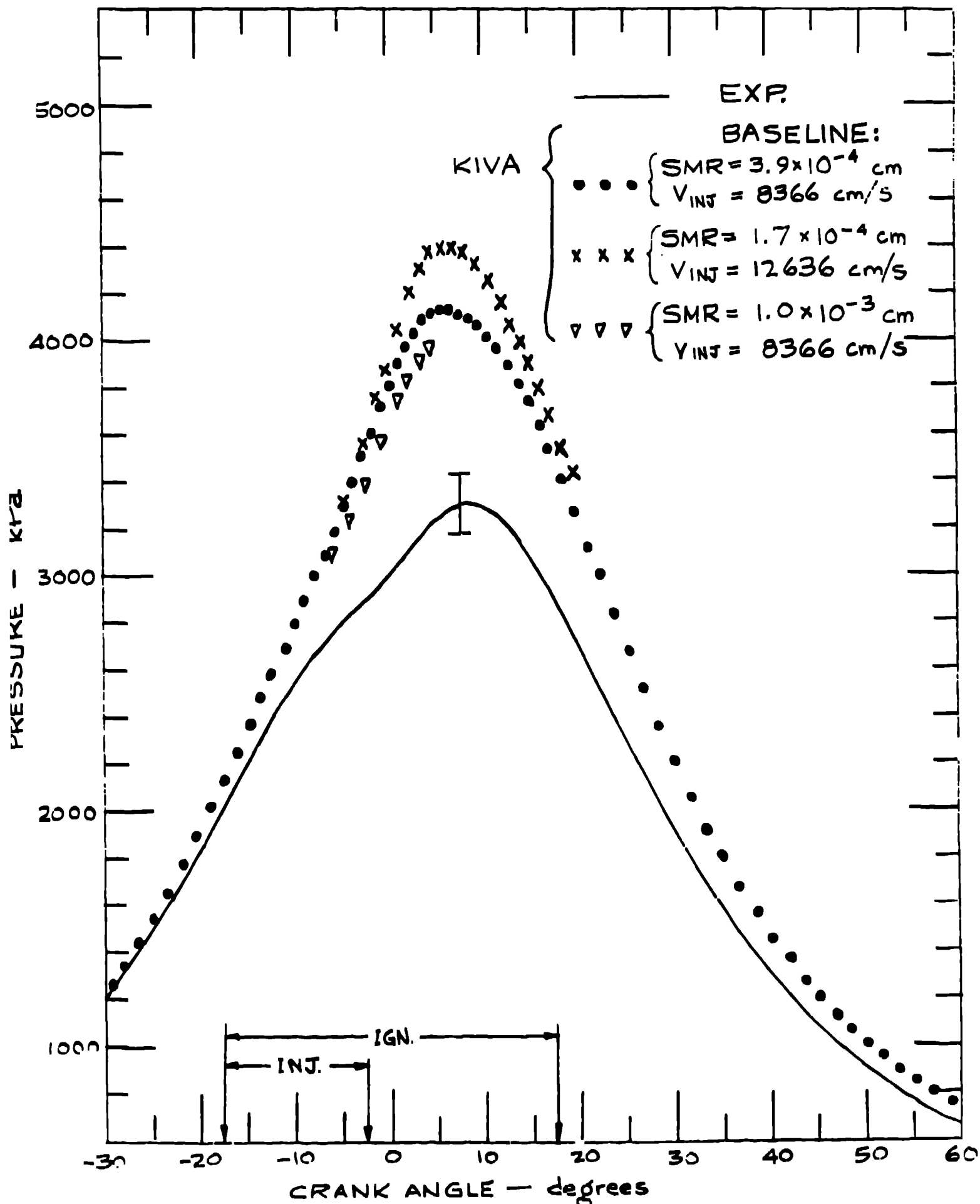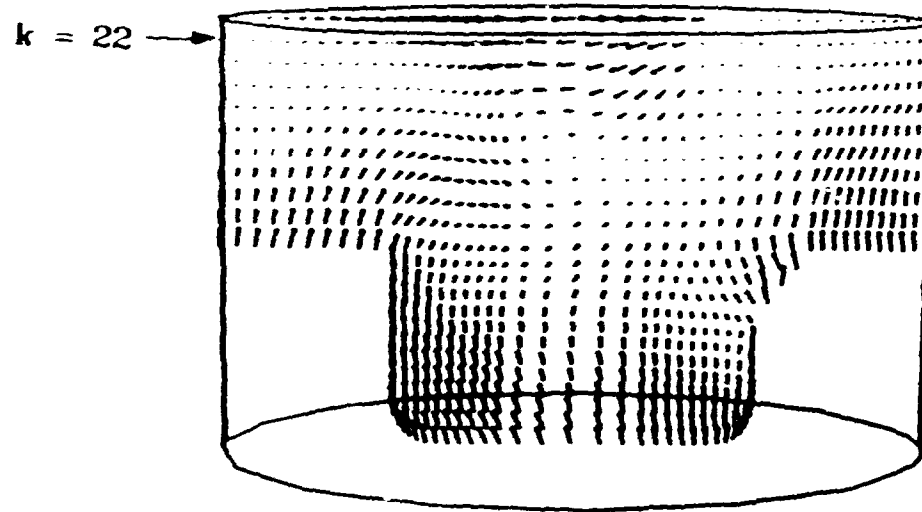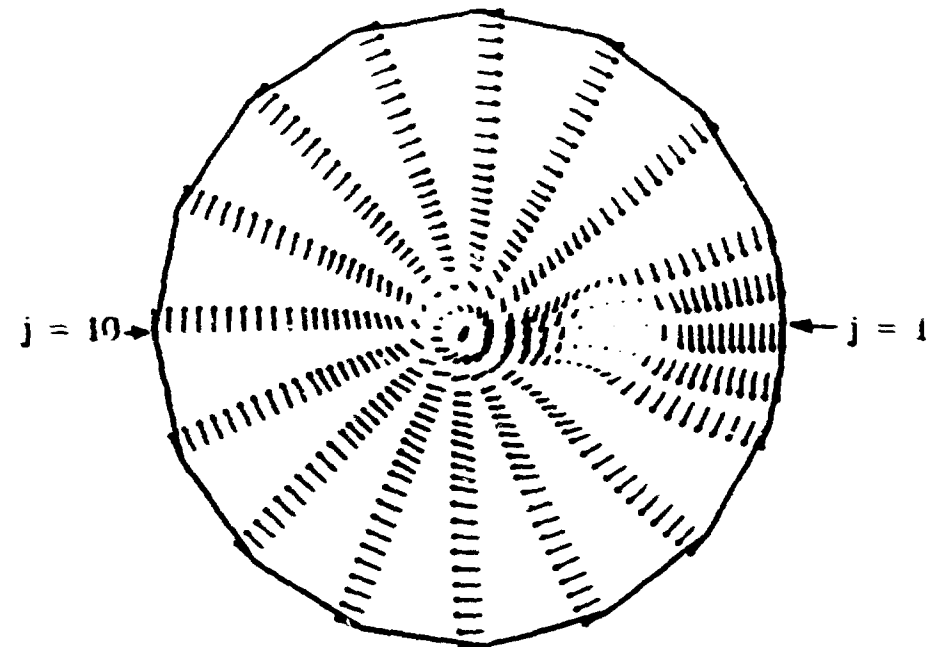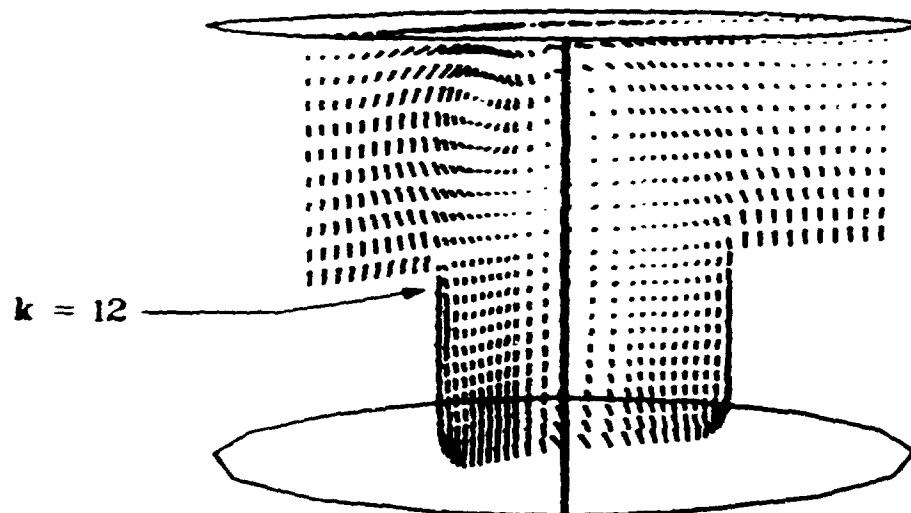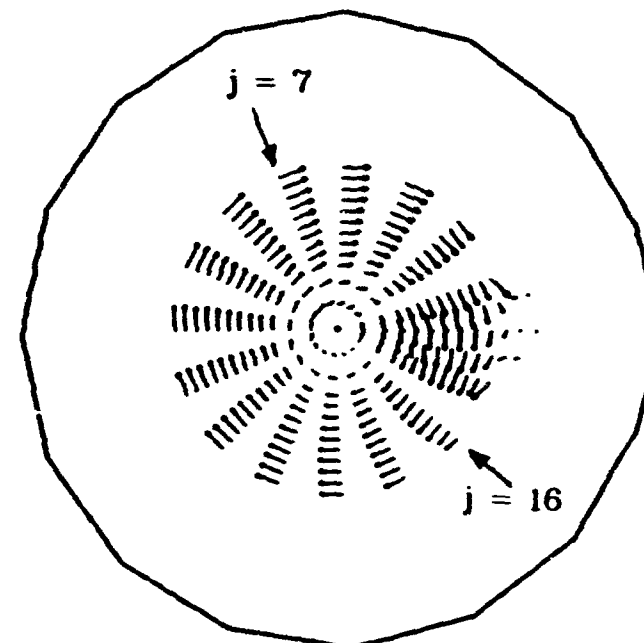
k = 12: u_{max} = 4540 cm/sec
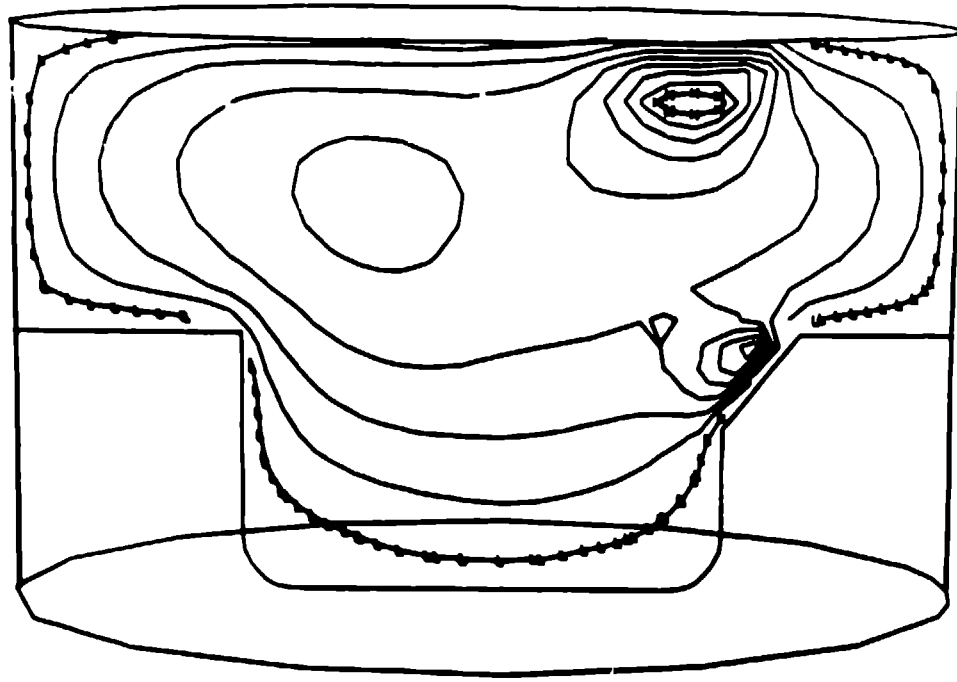
$j = 1 \, \alpha \, 10 : \quad H = 3.26 \times 10^{6} \, \frac{cm^2}{s^2} \, , \quad L = 4.46 \times 10^{5} \, \frac{cm^2}{s^2}$
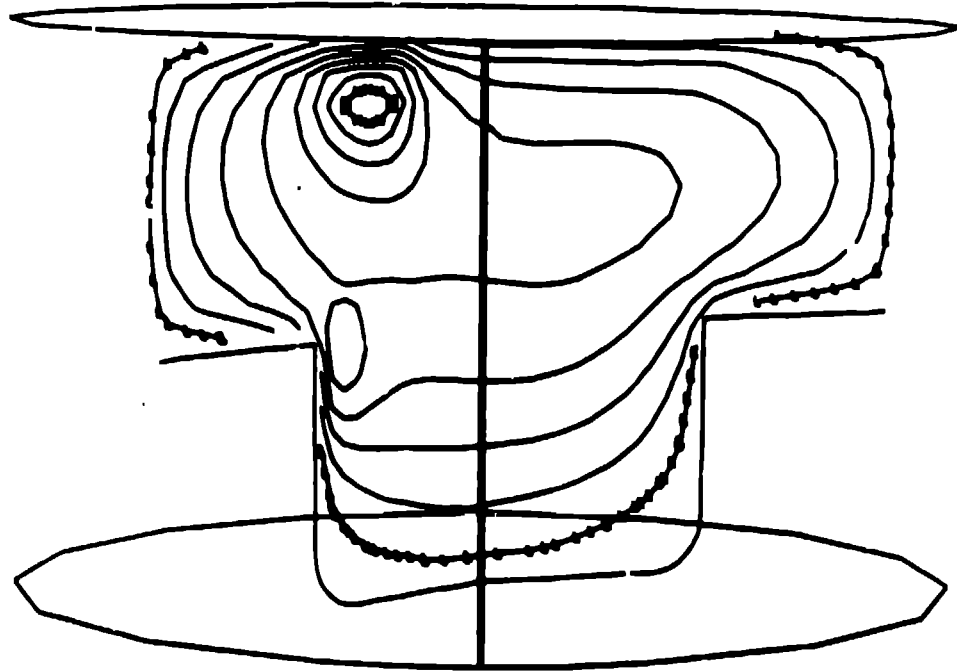
$j = 7 \, \alpha \, 16 : \quad H = 2.99 \times 10^{6} \, \frac{cm^2}{s^2} \, , \quad L = 4.20 \times 10^{5} \, \frac{cm^2}{s^2}$

Fig 23 Specific Turbulent Kinetic Energies at 58° BTDC

Fig 34

FUEL SPRAY AT 13° BTDC
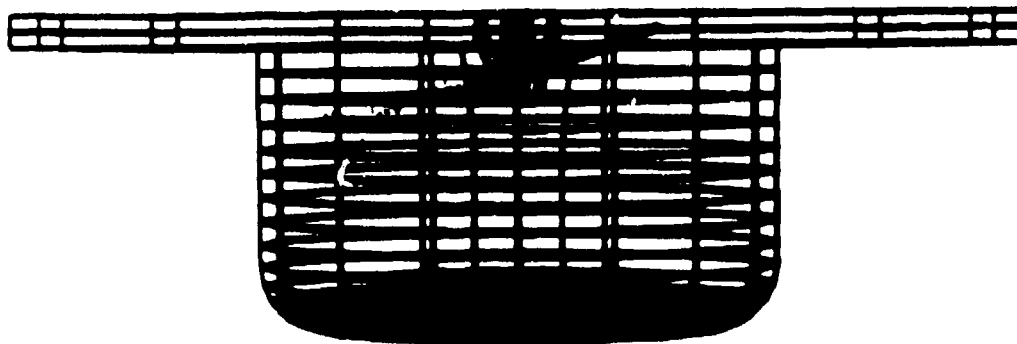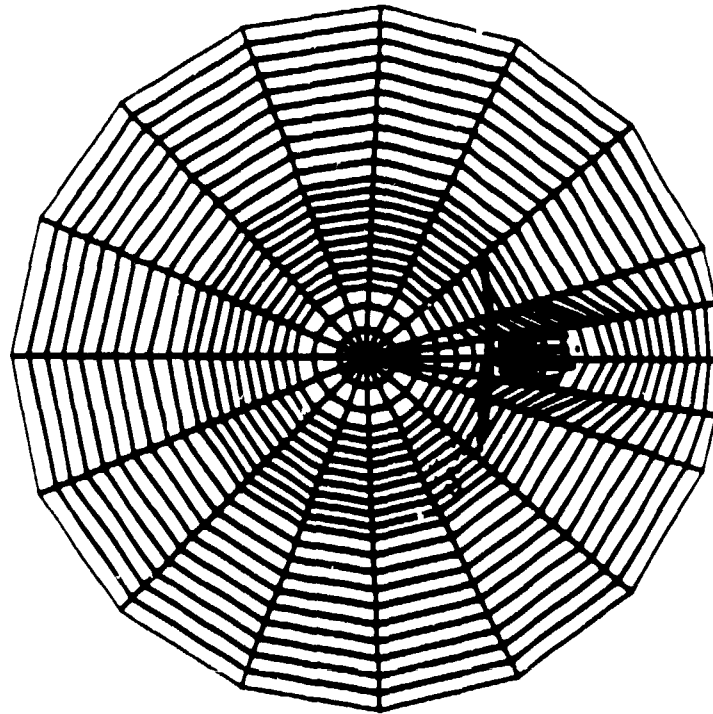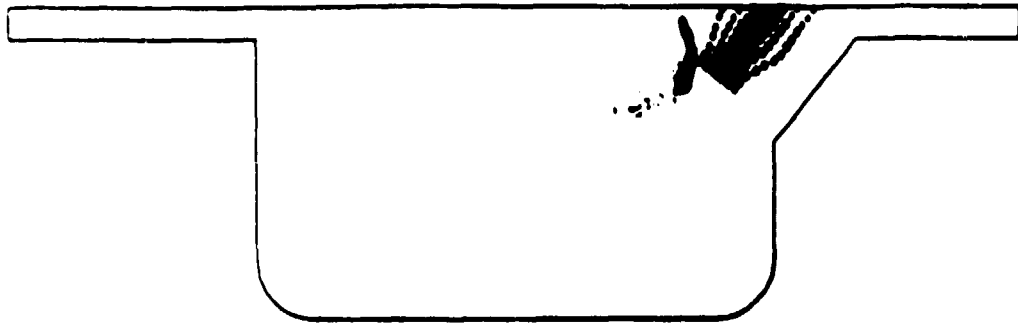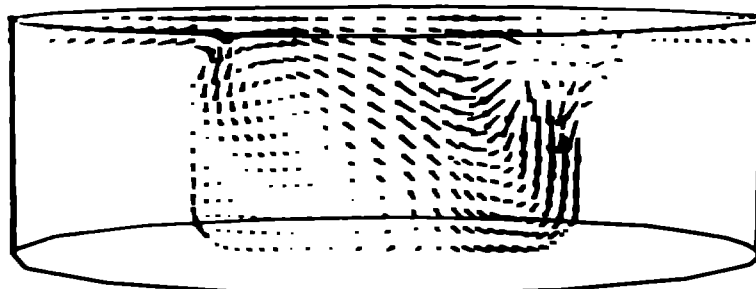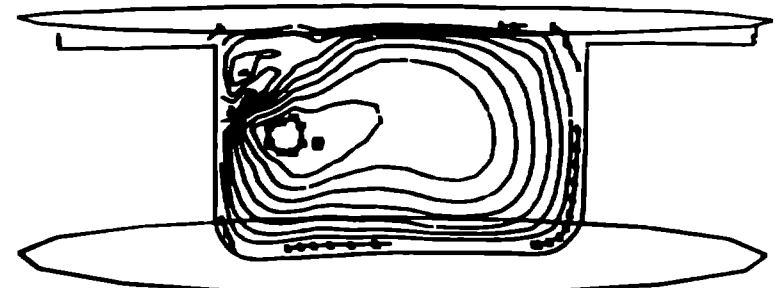
ELOCITY
IECTORS

UMAX = 2550 $^{cm}/_s$ UMAX = 2300 $^{cm}/_s$
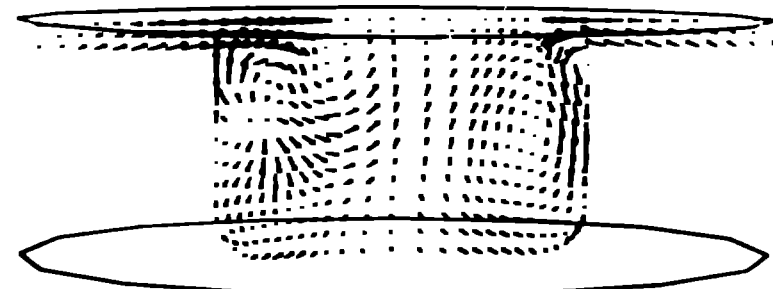
URBULENT
KINETIC
ENERGY
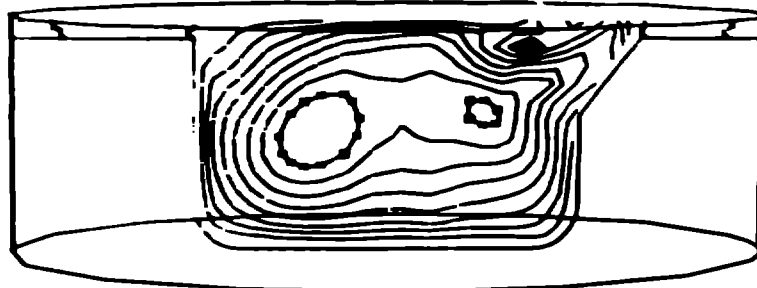
H=1.57×10$^-$ $\frac{cm^2}{s^2}$, L = 1.91×10^5 $\frac{cm^2}{s^2}$ H=1.60×10^6, L = 3.09×10^5 $\frac{cm^2}{s^2}$

LENGTH
SCALE
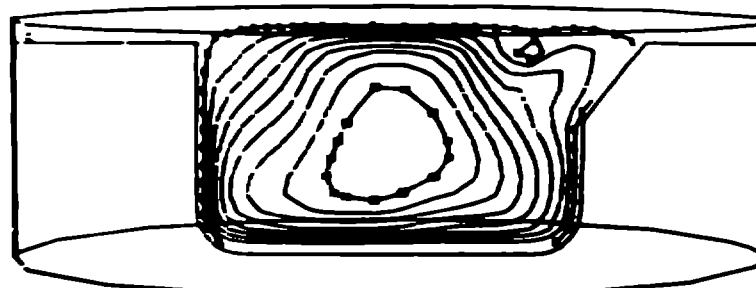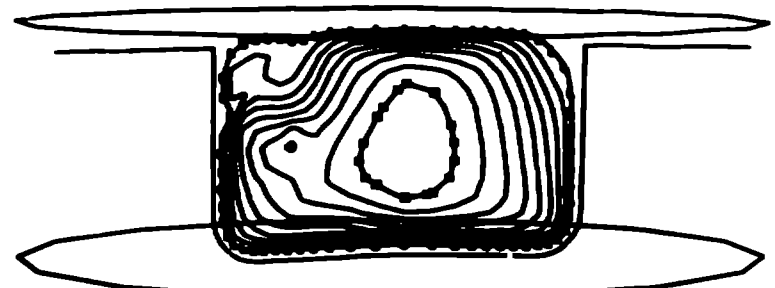
H = 2.06 cm, L = 0.23 cm   H = 2.05 cm, L = 0.36 cm

Fig 25 Velocity vector Plots and Contour Plots of Turbulent Kinetic
Energy and Length Scale at 13° BTDC.